



Contents lists available at ScienceDirect

# International Journal of Plasticity

journal homepage: [www.elsevier.com/locate/ijplas](http://www.elsevier.com/locate/ijplas)



## Phase-field approach for stress- and temperature-induced phase transformations that satisfies lattice instability conditions. Part 2. simulations of phase transformations Si I $\leftrightarrow$ Si II

Hamed Babaei<sup>a</sup>, Valery I. Levitas<sup>b,c,\*</sup>

<sup>a</sup> Iowa State University, Department of Aerospace Engineering, Ames, IA, 50011, USA

<sup>b</sup> Iowa State University, Departments of Aerospace Engineering, Mechanical Engineering, and Material Science and Engineering, Ames, IA, 50011, USA

<sup>c</sup> Ames Laboratory, Division of Materials Science and Engineering, Ames, IA, USA



### ARTICLE INFO

**Keywords:**

Phase-field approach  
Martensitic phase transformation  
Lattice instability condition  
Nanostructure

### ABSTRACT

A complete system of equations of the advanced phase-field theory for martensitic phase transformations (PTs) under a general stress tensor is presented. Theory includes a fully geometrically nonlinear formulation for the general case of finite elastic and transformational strains as well as anisotropic and different elastic properties of phases. Material parameters are calibrated, in particular, based on the crystal lattice instability conditions from atomistic simulations for martensitic PTs between cubic Si I and tetragonal Si II phases under complex triaxial compression-tension loading. A finite element algorithm and numerical procedure is developed and implemented in the code deal.II. Various 3D problems on lattice instabilities and following nanostructure evolution in single-crystal silicon are solved for compression in one direction under lateral stresses and analyzed. Strong effects of the stress states and local stress hysteresis on the interface width and nanostructure evolution are presented. In particular, the interface width diverges when lateral stress tends to the region in which instability stresses for direct and reverse PTs coincide. Direct and reverse transformations both occur in the unique homogeneous way without hysteresis, energy dissipation, and damage due to internal elastic stresses. Stress fields within a sample and especially within interfaces are determined and their effect on the nanostructure evolution is analyzed. Problems with definition of the elastic interfacial tension (stress) are analyzed. It is demonstrated that the instability stresses for initiation of the PTs are independent of the prescribed stress measure; however, this does not mean that PT will be completed at such stresses.

### 1. Introduction

In part 1 of this paper (Levitas (2018b)) the general phase-field approach (PFA) to stress- and temperature-induced martensitic phase transformations (PTs) is developed. This approach takes into account the crystal lattice instability conditions obtained in Levitas et al. (2017a,b) using molecular dynamics (MD) simulations. In the current paper:

(a) we specify and simplify the general theory; further study the new PFA analytically and numerically for homogeneous

\* Corresponding author. Iowa State University, Departments of Aerospace Engineering, Mechanical Engineering, and Material Science and Engineering, Ames, IA, 50011, USA.

E-mail addresses: [hbabaei@iastate.edu](mailto:hbabaei@iastate.edu) (H. Babaei), [vlevitas@iastate.edu](mailto:vlevitas@iastate.edu) (V.I. Levitas).

- deformation-transformation processes;
- (b) develop the finite element method (FEM) approach for solution of the coupled PFA and mechanics problem, and
  - (c) model various nontrivial nanostructures and phenomena during PTs between diamond cubic phase Si I and  $\beta$ -tin phase Si II under action of three stresses normal to the cubic faces.

In Section 2 we present a specific and simplified version of the general theory. Since the structural part of the interfacial stresses is found to be small in comparison with elastic interfacial stresses, they are neglected here. This slightly changes the expressions for the local and gradient parts of the Helmholtz free energy, the thermodynamic driving force for variation of the order parameter  $\eta$ , the lattice instability criteria and the material parameters in them obtained from MD simulations. The complete system of equations is formulated for two large-strain kinematic models, one based on interpolation of the transformation strain tensor and the other, on interpolation of the logarithmic transformation strain. The anisotropic elastic properties of the cubic Si I and tetragonal Si II are included in the model. The fifth-degree interpolation polynomial for all material properties that satisfied all formulated requirements are utilized.

In Section 3 we calibrate the model for cubic-tetragonal  $\text{Si I} \leftrightarrow \text{Si II}$  PTs using known experimental material properties and MD results from Levitas et al. (2017a,b). A serious problem was observed after initial calibration using the fifth-degree interpolation polynomials for all components of the transformations strain tensor. Strangely, the stress-order parameter curve for uniaxial loading exhibited a local minimum within the intermediate states  $0 < \eta < 1$ , where the stress fell far below the reverse PT instability stress. Such a plot results in an unphysical stationary microstructure, which contains incomplete Si II bands and corresponds to the minimum in the stress-strain curve. The problem can be resolved if the fourth-degree interpolation function is used for the transformation strain in the loading direction while keeping the fifth-degree polynomials for two lateral directions. For the logarithmic transformation strain-based model, the problem is resolved for a large arbitrary strain. However, for the transformation strain-based model, the problem is fully resolved only for small strain. For the finite strains, small non-monotonicity of the stress-strain curve during the PT is observed, leading to more complex instability behavior which is discussed in Section 7.

Simulation results are presented in Sections 4–7. The effect of the lateral stress on nanostructure evolution during compression is analyzed in Section 4. Because the increase in tensile lateral stress reduces the stress hysteresis to zero, the interface width increases and tends to infinity. For such lateral stresses,  $\text{Si I} \leftrightarrow \text{Si II}$  PTs occur in the unique homogeneous way without nucleation and growth, hysteresis, energy dissipation, and damage due to internal elastic stresses. These properties are ideal for various PT-related engineering applications. If one increases the tensile lateral stresses starting with two-phase structure under prescribed strain, the nanostructure continuously transforms to the homogenous intermediate structure. There is an infinite number (continuum) of the homogeneous intermediate phases along the homogeneous  $\text{Si I} \leftrightarrow \text{Si II}$  path which are in indifferent thermodynamic equilibrium. These results are in good agreement with the MD results in Levitas et al. (2017a). The effect of the hysteresis width of the nanostructure evolution and the distribution of the driving force for PT was analyzed in Section 5. Due to the large transformation strain and internal elastic stresses, for the relatively small hysteresis, Si II evolve not only by growth of complete Si II regions, but also by loss of stability of the residual Si I and its quasi-homogeneous evolution toward Si I. Also, the total width of all phase interfaces becomes comparable to the sample size; thus interfaces overlap and fill the entire sample until completing the PT. Stresses in the sample, with focus on the stresses within interfaces, were studied in Section 6. A detailed analysis of the lattice instability conditions under prescribed Cauchy and first Piola–Kirchhoff stress is presented in Section 7. It is shown that the lattice instability conditions (i.e. deviation of  $\eta$  from 0 and 1) are indeed independent of whether the Cauchy or the first Piola–Kirchhoff stresses are prescribed. However, this does not mean that PT will be completed at such stresses. The second instability points, which depend on the prescribed stress measure, appear due to geometric nonlinearity after which PT completes. Section 8 contains concluding remarks.

Vectors and tensors are designated with boldface symbols. We designate contractions of tensors  $\mathbf{A} = \{A_{ij}\}$  and  $\mathbf{B} = \{B_{ji}\}$  over one and two indices as  $\mathbf{A} \cdot \mathbf{B} = \{A_{ij} B_{jk}\}$  and  $\mathbf{A}: \mathbf{B} = A_{ij} B_{ji}$ . The transpose of  $\mathbf{A}$  is  $\mathbf{A}^T$ , the symmetrized tensor  $\mathbf{A}$  is  $\mathbf{A}_s$  and  $I$  is the unit tensor;  $\nabla_0$  is the gradient operator with respect to the undeformed state.

## 2. Complete system of equations

The phase-field theory developed in Levitas (2018b) is simplified and specified for the cubic-to-tetragonal  $\text{Si I} \leftrightarrow \text{Si II}$  PTs. Thus, the structural interfacial stresses will be neglected because the elastic interfacial stresses are found to be much larger, simplifying simulations.

Due to a lack of the higher-order elastic constants in the literature we considered the available second-order constants only. Because the elastic constants do not contribute to the instability criteria, this simplification does not hurt our main points of study. However, stress-strain curves before PT are obviously affected by neglecting the higher-order elasticity. In addition to large strain formulations, equations will also be presented in the small strain approximation to make them more comprehensible for the broader audience.

### 2.1. Kinematics

The motion of the elastic material with PTs will be described by a continuous vector function  $\mathbf{r} = \mathbf{r}(\mathbf{r}_0, t)$ , where  $\mathbf{r}_0$  and  $\mathbf{r}$  are the positions of points in the reference (undeformed)  $\Omega_0$  and the current (deformed)  $\Omega$  configurations, respectively;  $t$  is the time. The deformation gradient  $\mathbf{F} = \frac{\partial \mathbf{r}}{\partial \mathbf{r}_0} = \nabla_0 \mathbf{r}$  can be multiplicatively decomposed

$$\mathbf{F} = \mathbf{F}_e \cdot \mathbf{U}_t, \quad (1)$$

into an elastic part and a symmetric (rotation-free) transformational part. The intermediate stress-free configuration, designated as  $\Omega_t$ , is characterized by  $\mathbf{U}_t$  after elastic unloading from  $\Omega$  to zero stresses. The Jacobian determinants, which describe ratios of volumes  $V$  in the corresponding configurations, are

$$J = \frac{dV}{dV_0} = \det \mathbf{F}; \quad J_e = \frac{dV}{dV_t} = \det \mathbf{F}_e; \quad J_t = \frac{dV_t}{dV_0} = \det \mathbf{U}_t. \quad (2)$$

The transformational deformation gradient is expressed in two different ways (Levitas (2018b)), both in a way that allows us to satisfy the lattice instability conditions obtained from MD simulations. First, based on the interpolation of the transformation strain:

$$\mathbf{U}_t(\eta) = \mathbf{I} + \boldsymbol{\varepsilon}_t \circ \boldsymbol{\varphi}(\mathbf{a}_\varepsilon, \mathbf{w}_\varepsilon, \eta);$$

$$\boldsymbol{\varphi} := [\mathbf{a}_\varepsilon \eta^2 + (10t - 3\mathbf{a}_\varepsilon + \mathbf{w}_\varepsilon) \eta^3 + (3\mathbf{a}_\varepsilon - 2\mathbf{w}_\varepsilon - 15t) \eta^4 + (6t - \mathbf{a}_\varepsilon + \mathbf{w}_\varepsilon) \eta^5], \quad (3)$$

where  $\boldsymbol{\varepsilon}_t = \mathbf{U}_t(1) - \mathbf{I}$  is the transformation strain after complete transformation from the parent phase  $P_0$  to the product phase  $P_1$ ;  $\boldsymbol{\varphi}$  (and consequently,  $\mathbf{a}_\varepsilon$ ,  $\mathbf{w}_\varepsilon$ ,  $t$ ) are matrices (not second-rank tensors), which have the same non-zero components and symmetry as  $\boldsymbol{\varepsilon}_t$  in the coordinate system of crystal lattice of  $P_1$ ; these matrices were defined in Levitas (2018b) and specified in Section 3.4; all non-zero components of matrix  $t$  are equal to one. The Hadamard product is defined as  $\boldsymbol{\varepsilon}_t \circ \boldsymbol{\varphi} := \{\varepsilon_t^{ij} \varphi^{ij}\}$  with no summation over  $i$  and  $j$ . Phase transformation is described by the order parameter  $\eta$  with  $\eta = 0$  for  $P_0$  and  $\eta = 1$  for  $P_1$ . For transformations between cubic and tetragonal phases Si I  $\leftrightarrow$  Si II, all matrices are defined in the cubic axes of Si I and all non-diagonal components are zero.

Second, the exponential-logarithmic representation that generalizes the one presented in Tůma and Stupkiewicz (2016); Tůma et al. (2016) and separates volumetric and deviatoric parts (see Levitas (2018b)):

$$\mathbf{U}_t(\eta) = \exp\{\ln \mathbf{U}_t(0) + \mathbf{H}(\eta)\}; \quad \text{with } \mathbf{H}(1) = \ln \mathbf{U}_t(1) - \ln \mathbf{U}_t(0) \quad \& \quad \mathbf{H}(0) = 0, \quad (4)$$

where the tensor  $\mathbf{H}(\eta)$  is interpolated as

$$\mathbf{H}(\eta) = H_v(1) \mathbf{I} \boldsymbol{\varphi}_v(a_v, w_v, \eta) + \mathbf{H}_{dd}(1) \circ \boldsymbol{\varphi}_{dd}(\mathbf{a}_d, \mathbf{w}_d, \eta); \quad (5)$$

$$H_v(1) = \frac{1}{3} \operatorname{tr} \mathbf{H}(1) = \frac{1}{3} \ln \frac{J_t(1)}{J_t(0)}; \quad \mathbf{H}_{dd}(1) = \mathbf{H}(1) - H_v(1) \mathbf{I}; \quad (6)$$

$$\operatorname{tr} [\mathbf{H}_{dd}(1) \circ \boldsymbol{\varphi}(\mathbf{a}_d, \mathbf{w}_d, \eta)] = 0 \quad \forall \eta. \quad (7)$$

Thus, the tensor  $\mathbf{H}(\eta)$  consists of a spherical part  $H_v$ , which solely determines the volumetric transformation strain, and a diagonal deviatoric  $\mathbf{H}_{dd}$  part, which do not affect the volumetric transformation strain.

Here, the main motivation for using the logarithmic expression is to separate the contributions due to the change of volume and shape to the driving force for PT and lattice instability conditions.

The Lagrangian total, elastic, and transformation strains are respectively given by

$$\mathbf{E} = \frac{1}{2} (\mathbf{F}^t \cdot \mathbf{F} - \mathbf{I}); \quad \mathbf{E}_e = \frac{1}{2} (\mathbf{F}_e^t \cdot \mathbf{F}_e - \mathbf{I}); \quad \mathbf{E}_t = \frac{1}{2} (\mathbf{U}_t \cdot \mathbf{U}_t - \mathbf{I}); \quad (8)$$

for small strains, they simplify to

$$\mathbf{E} \simeq \boldsymbol{\varepsilon} = (\nabla \mathbf{u})_s = \boldsymbol{\varepsilon}_e + \bar{\boldsymbol{\varepsilon}}_t; \quad (9)$$

$$\bar{\boldsymbol{\varepsilon}}_t = \boldsymbol{\varepsilon}_t \circ \boldsymbol{\varphi}(\mathbf{a}_\varepsilon, \mathbf{w}_\varepsilon, \eta), \quad (10)$$

where  $\mathbf{u}$  is the displacement vector and subscript 0 in the gradient is omitted due to the negligible difference between the reference and actual configurations. With interpolation for the transformation strain and for the logarithmic transformation strain, both kinematic models coincide. Note, as it was shown in Basak and Levitas (2017), that the elastic interfacial stresses depend on the second order terms of  $\boldsymbol{\varepsilon}_t$  in the Taylor expansion of  $\mathbf{E}_t$ , which are neglected in the traditional small strain approach. Because these stresses are quite large, this demonstrates the danger of using small strain approximation.

## 2.2. Helmholtz free energy

The Helmholtz free energy per unit reference volume can be written as

$$\bar{\psi}(\mathbf{F}, \eta, \theta, \nabla_0 \eta) = J_t \psi^e + \psi^\theta + \psi^\nabla, \quad (11)$$

where  $\psi^e$  is the elastic energy per unit volume in the intermediate configuration  $\Omega_t$ , which is the reference configuration for the elasticity rule;  $\psi^\theta$  is the thermal energy, which includes the energy barrier between phases as well as the thermal driving force for phase transformation; and  $\psi^\nabla$  is the gradient energy which penalizes interfaces. In contrast with Levitas (2018b), we consider all energies per unit reference volume rather than per unit mass.

Also, because the interfacial stresses are neglected, the gradient and double well energies are not multiplied by  $J$ .

The simplest elastic energy for an anisotropic crystal is expressed as (Lekhnitskii (1963))

$$\psi^e = \frac{1}{2} \mathbf{E}_e : \mathbf{C} : \mathbf{E}_e = \frac{1}{2} C^{ijkl} E_e^{ij} E_e^{kl} = \frac{1}{2} \sum_{n=1}^3 [\lambda^n (E_e^{nn})^2 + 2\mu^n E_e^{nn} E_e^{kk} + 4\nu^n E_e^{nk} E_e^{kn}]. \quad (12)$$

The fourth rank elastic moduli for orthotropic materials with three orthogonal symmetry planes are considered as

$$C^{ijkl} = \sum_{n=1}^3 [\lambda^n \delta^{in} \delta^{jn} \delta^{kn} \delta^{ln} + \mu^n (\delta^{in} \delta^{jn} \delta^{kl} + \delta^{ij} \delta^{kn} \delta^{ln}) + \nu^n (\delta^{in} \delta^{jk} \delta^{ln} + \delta^{jn} \delta^{ik} \delta^{ln} + \delta^{in} \delta^{jl} \delta^{kn} + \delta^{jn} \delta^{il} \delta^{kn})], \quad (13)$$

where constants  $\lambda^n$ ,  $\mu^n$  and  $\nu^n$  can be expressed in terms of nine independent elastic constants as

$$\begin{aligned} \lambda^1 &= C^{11} + C^{23} + 2C^{44} - (C^{12} + C^{13} + 2C^{55} + 2C^{66}), \\ \lambda^2 &= C^{22} + C^{13} + 2C^{55} - (C^{12} + C^{23} + 2C^{44} + 2C^{66}), \\ \lambda^3 &= C^{33} + C^{12} + 2C^{66} - (C^{13} + C^{23} + 2C^{44} + 2C^{55}), \\ 2\mu^1 &= C^{12} + C^{13} - C^{23}, \quad 2\nu^1 = C^{55} + C^{66} - C^{44}, \\ 2\mu^2 &= C^{12} + C^{23} - C^{13}, \quad 2\nu^1 = C^{44} + C^{66} - C^{55}, \\ 2\mu^3 &= C^{13} + C^{23} - C^{12}, \quad 2\nu^1 = C^{44} + C^{55} - C^{66}. \end{aligned} \quad (14)$$

However, two of the symmetry planes are equivalent in the case of materials with tetragonal crystal lattices. Therefore,  $C^{11} = C^{22}$ ,  $C^{13} = C^{23}$  and  $C^{44} = C^{55}$ , so that Eq. (14) simplifies to

$$\begin{aligned} \lambda^1 &= \lambda^2 = \lambda^3 = C^{11} - (C^{12} + 2C^{66}), \\ \lambda^3 &= C^{33} + C^{12} + 2C^{66} - 2(C^{13} + 2C^{44}), \\ 2\mu^1 &= 2\mu^2 = 2\mu^3 = C^{12}, \quad 2\mu^3 = 2C^{13} - C^{12}, \\ 2\nu^1 &= 2\nu^2 = C^{66}, \quad 2\nu^3 = 2C^{44} - C^{66}. \end{aligned} \quad (15)$$

Besides, all three orthogonal symmetry planes are equivalent for materials with cubic crystal lattices, resulting in  $C^{11} = C^{22} = C^{33}$ ,  $C^{13} = C^{23} = C^{13}$  and  $C^{44} = C^{55} = C^{66}$ , so that Eq. (14) reads to

$$\begin{aligned} \lambda^1 &= \lambda^2 = \lambda^3 = C^{11} - C^{12} - 2C^{44}, \\ 2\mu^1 &= 2\mu^2 = 2\mu^3 = C^{12}, \\ 2\nu^1 &= 2\nu^2 = 2\nu^3 = C^{44}. \end{aligned} \quad (16)$$

During the PT, the elastic constants  $\lambda^n$ ,  $\mu^n$  and  $\nu^n$  for the three orthogonal directions are interpolated as

$$\lambda^n = \lambda_0^n + (\lambda_1^n - \lambda_0^n)\varphi_e(\eta); \quad \mu^n = \mu_0^n + (\mu_1^n - \mu_0^n)\varphi_e(\eta); \quad \nu^n = \nu_0^n + (\nu_1^n - \nu_0^n)\varphi_e(\eta), \quad (17)$$

with  $\lambda_0^n$ ,  $\mu_0^n$ ,  $\nu_0^n$  and  $\lambda_1^n$ ,  $\mu_1^n$ ,  $\nu_1^n$  for the elastic constants of  $P_0$  and  $P_1$ , respectively. The corresponding interpolation function is (Levitas (2018b)):

$$\varphi_e(\eta) = \eta^3(10 - 15\eta + 6\eta^2). \quad (18)$$

The first and second derivatives of this function at  $\eta = 0$  and 1 are zero. This function is used to prevent the term due to change in elastic moduli, which includes nonlinear elastic energy, from contributing to the instability criteria, which were found to be linear in stresses by MD simulations for Si I  $\leftrightarrow$  Si II PTs (Levitas et al. (2017a, b)).

The thermal part of the free energy is

$$\psi^\theta = A\eta^2(1 - \eta)^2 + \Delta\psi^\theta(3\eta^2 - 2\eta^3) = (A + 3\Delta\psi^\theta)\eta^2(1 - \eta)^2 + \Delta\psi^\theta\eta^3(4 - 3\eta), \quad (19)$$

where  $A$  is a material parameter,  $\Delta\psi^\theta$  is the difference between the thermal free energy of  $P_1$  and  $P_0$ , and combination  $A + 3\Delta\psi^\theta$  is the magnitude of the double-well barrier between  $P_0$  and  $P_1$ , which represents a barrier in the criterion for  $P_0$  to  $P_1$  PT in Eqs. (29) and (30).

This is a particular case of the general expression for  $\psi^\theta$  obtained by considering traditional  $a = 3$  in Eq. (58) in Levitas (2018b), because there are no data for choosing another value.

The gradient part of the free energy is expressed as

$$\psi^\nabla = \frac{\beta}{2} |\nabla_0 \eta|^2, \quad (20)$$

where  $\beta$  is a constant coefficient. In contrast to Levitas (2018b), the gradient is defined in the reference configuration rather than the actual configuration, again due to the neglected interfacial stresses.

The following simplifications are valid for small strains:  $J_t \simeq 1$ ,  $\mathbf{E}_e \simeq \boldsymbol{\varepsilon}_e$ , and  $\nabla_0 \simeq \nabla$ .

### 2.3. The first Piola-Kirchhoff and Cauchy stress tensors

The first Piola-Kirchhoff stress and the Cauchy stress have the following expressions (Levitas (2018b)):

$$\mathbf{P} = J_t \mathbf{F}_e \cdot \frac{\partial \psi^e}{\partial \mathbf{E}_e} \cdot \mathbf{U}_t^{-1} = J_t \mathbf{F}_e \cdot \mathbf{C} : \mathbf{E}_e \cdot \mathbf{U}_t^{-1};$$

$$\sigma = J^{-1} \mathbf{P} \cdot \mathbf{F}^T = J_t \mathbf{F}_e \cdot \frac{\partial \psi^e}{\partial \mathbf{E}_e} \cdot \mathbf{F}_e^T = J_e^{-1} \mathbf{F}_e \cdot \mathbf{C} : \mathbf{E}_e \cdot \mathbf{F}_e^T; \quad (21)$$

for *small strains* they simplify to

$$\mathbf{P} \simeq \sigma \simeq \rho \frac{\partial \psi^e}{\partial \varepsilon_e} = \mathbf{C} : \varepsilon_e. \quad (22)$$

#### 2.4. Ginzburg-Landau equation

The evolution of the order parameter and corresponding martensitic nanostructure can be described by the Ginzburg-Landau equation, which represents a linear relationship between the rate of change of the order parameter,  $\dot{\eta}$ , and the conjugate generalized thermodynamic force,  $X$ :

$$\dot{\eta} = LX = L \left( -\frac{\partial \bar{\Psi}}{\partial \eta} \Big|_E + \nabla_0 \cdot \left( \frac{\partial \bar{\Psi}}{\partial \nabla_0 \eta} \right) \right), \quad (23)$$

where  $L$  is the kinetic coefficient. Substituting the free energy Eq. (11) into Eq. (23) results in the more explicit but still compact form of the Ginzburg-Landau equation in the reference configuration

$$\dot{\eta} = LX = L \left( \mathbf{P}^T \cdot \mathbf{F}_e : \frac{\partial \mathbf{U}_t}{\partial \eta} - J_t \frac{\partial \psi^e}{\partial \eta} \Big|_{E_e} - J_t \psi^e \mathbf{U}_t^{-1} : \frac{\partial \mathbf{U}_t}{\partial \eta} - \frac{\partial \psi^\theta}{\partial \eta} + \beta \nabla_0^2 \eta \right), \quad (24)$$

and for *small strains* it reduces to

$$\dot{\eta} = LX = L \left( \sigma : \frac{\partial \bar{\varepsilon}_t}{\partial \eta} - \rho \frac{\partial (\psi^e + \psi^\theta)}{\partial \eta} + \beta \nabla^2 \eta \right). \quad (25)$$

#### 2.5. Equilibrium equation

The mechanical equilibrium equation is presented in the reference configuration as

$$\nabla_0 \cdot \mathbf{P} = \mathbf{0}. \quad (26)$$

For *small strains* the equilibrium equation reduces to  $\nabla \cdot \sigma = \mathbf{0}$ .

#### 2.6. Crystal lattice instability criteria

By definition, if a spontaneous deviation of the order parameter from the thermodynamic equilibrium values  $\hat{\eta} = 0$  or  $1$  is thermodynamically admissible under the prescribed boundary conditions, then the equilibrium is unstable. As elaborated in [Levitas \(2013, 2018b\)](#), the general PFA criterion for the instability of the equilibrium phase  $\hat{\eta}$  can be presented as:

$$\frac{\partial X(\mathbf{P}, \mathbf{F}_e, \hat{\eta})}{\partial \eta} = \mathbf{P}^T \cdot \mathbf{F}_e : \frac{\partial^2 \mathbf{U}_t}{\partial \eta^2} - J_t \frac{\partial^2 \psi^e}{\partial \eta^2} \Big|_{E_e} - J_t \psi^e \mathbf{U}_t^{-1} : \frac{\partial^2 \mathbf{U}_t}{\partial \eta^2} - \frac{\partial^2 \psi^\theta}{\partial \eta^2} \geq 0, \quad \eta = \hat{\eta}. \quad (27)$$

While Eq. (27) was obtained at fixed  $\mathbf{P}$ , it is proven in [Levitas \(2018b\)](#) that the result does not change if one fixes any stress measure. For *small strains* Eq. (27) reduces to

$$\frac{\partial X(\sigma, \varepsilon_e, \hat{\eta})}{\partial \eta} = \sigma : \frac{\partial^2 \bar{\varepsilon}_t}{\partial \eta^2} - \frac{\partial^2 \psi^e}{\partial \eta^2} \Big|_{E_e} - \frac{\partial^2 \psi^\theta}{\partial \eta^2} \geq 0, \quad \eta = \hat{\eta}. \quad (28)$$

By substituting all of the terms in Eq. (27), expressing the first Piola-Kirchhoff stress in terms of Cauchy stress, and neglecting shear stresses, one obtains the criteria for direct and reverse PTs for both kinematic models (Eqs. (128-131) in [Levitas \(2018b\)](#)). The difference in Jacobians is caused by neglecting Jacobian  $J$  in the expression for thermal energy due to neglecting the interfacial stresses. First, considering the kinematic model based on the transformation strain  $\varepsilon_t$ , we obtain

$$\begin{aligned} P_0 \rightarrow P_1: \quad & \frac{\partial X}{\partial \eta} \Big|_{\eta=0} \geq 0 \quad \Rightarrow \quad \left( \sigma - \frac{\psi^e}{J_e} \mathbf{I} \right) : \varepsilon_t \circ \mathbf{a}_\varepsilon - \frac{1}{J_e} (A + 3\Delta\psi^\theta) \geq 0; \\ P_1 \rightarrow P_0: \quad & \frac{\partial X}{\partial \eta} \Big|_{\eta=1} \geq 0 \quad \Rightarrow \quad \left( \sigma - \frac{\psi^e}{J_e} \mathbf{I} \right) : \mathbf{U}_t^{-1}(1) \cdot \varepsilon_t \circ \mathbf{w}_\varepsilon - \frac{1}{J} (A - 3\Delta\psi^\theta) \geq 0. \end{aligned} \quad (29)$$

Second, for the logarithmic transformation strain measure, one has

$$\begin{aligned} P_0 \rightarrow P_1: & \left. \frac{\partial X}{\partial \eta} \right|_{\eta=0} \geq 0 \Rightarrow \left( \sigma_0 - \frac{\psi^e}{J_e} \right) \ln(J_t(1)) a_v + \mathbf{S} : \{\mathbf{H}_{dd}(1) \circ \mathbf{a}_{dd}\} - \frac{1}{J_e} (A + 3\Delta\psi^\theta) \geq 0; \\ P_1 \rightarrow P_0: & \left. \frac{\partial X}{\partial \eta} \right|_{\eta=1} \geq 0 \Rightarrow \left( \sigma_0 - \frac{\psi^e}{J_e} \right) \ln(J_t(1)) w_v + \mathbf{S} : \{\mathbf{H}_{dd}(1) \circ \mathbf{w}_{dd}\} - \frac{1}{J} (A - 3\Delta\psi^\theta) \geq 0, \end{aligned} \quad (30)$$

where  $\sigma_0$  and  $\mathbf{S}$  are the spherical and deviatoric parts of the Cauchy stress tensor, respectively. Let us find more explicit expressions for Eqs. (29) and (30).

The term  $\psi^e$  can be neglected from here on for two reasons. First, the elastic energy is an order of magnitude smaller than the stresses. Second,  $\psi^e$  is a nonlinear expression of the stress components; however, the MD simulations shows that the instability criteria are linear in stresses. For the next step, we either consider loading three stresses  $\sigma_i$  normal to the cubic faces or neglect some geometrically nonlinear terms related to the contribution of the shear stresses to the instability condition (see Levitas et al. (2017b)). Elaborating the first terms in Eq. (29) for cubic to tetragonal PT and taking into account that  $\varepsilon_{t2} = \varepsilon_{t1}$  due to tetragonal symmetry, we obtain the simplified version of Eq. (29) as

$$\begin{aligned} P_0 \rightarrow P_1: & (\sigma_1 + \sigma_2) \varepsilon_{t1} a_{\varepsilon 1} + \sigma_3 \varepsilon_{t3} a_{\varepsilon 3} \geq \frac{1}{J_e} (A + 3\Delta\psi^\theta); \\ P_1 \rightarrow P_0: & (\sigma_1 + \sigma_2) \frac{\varepsilon_{t1} w_{\varepsilon 1}}{1 + \varepsilon_{t1}} + \frac{\sigma_3 \varepsilon_{t3} w_{\varepsilon 3}}{1 + \varepsilon_{t3}} \geq \frac{1}{J} (A - 3\Delta\psi^\theta). \end{aligned} \quad (31)$$

Next, elaborating the second terms in Eq. (30) using constraints in Eq. (7), the instability criteria for the logarithmic model simplify to

$$\begin{aligned} P_0 \rightarrow P_1: & \sigma_0 \ln(J_t(1)) a_v + (2\sigma_3 - \sigma_1 - \sigma_2) H_{dd}^{33}(1) a_d / 2 \geq \frac{1}{J_e} (A + 3\Delta\psi^\theta); \\ P_1 \rightarrow P_0: & \sigma_0 \ln(J_t(1)) w_v + (2\sigma_3 - \sigma_1 - \sigma_2) H_{dd}^{33}(1) w_d / 2 \geq \frac{1}{J} (A - 3\Delta\psi^\theta). \end{aligned} \quad (32)$$

For small strains, the criteria for both versions coincide:

$$\begin{aligned} P_0 \rightarrow P_1: & (\sigma_1 + \sigma_2) \varepsilon_{t1} a_{\varepsilon 1} + \sigma_3 \varepsilon_{t3} a_{\varepsilon 3} \geq (A + 3\Delta\psi^\theta); \\ P_1 \rightarrow P_0: & (\sigma_1 + \sigma_2) \varepsilon_{t1} w_{\varepsilon 1} + \sigma_3 \varepsilon_{t3} w_{\varepsilon 3} \geq (A - 3\Delta\psi^\theta). \end{aligned} \quad (33)$$

### 3. PFA calibration using MD results and stress-order parameter and stress-strain curves

The following material parameters are used (Hennig et al. (2010); Levitas et al. (2003)):  $L = 2600 \text{ (Pa.s)}^{-1}$ ,  $\beta = 2.59 \times 10^{-10} \text{ N}$ ,  $C_0^{11} = C_0^{22} = C_0^{33} = 167.5 \text{ GPa}$ ,  $C_0^{44} = C_0^{55} = C_0^{66} = 80.1 \text{ GPa}$ ,  $C_1^{11} = C_1^{22} = 174.76 \text{ GPa}$ ,  $C_1^{33} = 136.68 \text{ GPa}$ ,  $C_1^{44} = C_1^{55} = 60.24 \text{ GPa}$ ,  $C_1^{66} = 42.22 \text{ GPa}$ ,  $C_1^{12} = 102 \text{ GPa}$ ,  $C_1^{13} = C_1^{23} = 68 \text{ GPa}$ .

The thermal driving force for PT,  $\Delta\psi^\theta$ , the transformation strain,  $\varepsilon_t$ , and the double-well barrier constant,  $A$ , along with the constants in the interpolation function for transformation strain,  $a_{\varepsilon 1}$ ,  $a_{\varepsilon 3}$ ,  $w_{\varepsilon 1}$ , and  $w_{\varepsilon 3}$  within the transformation strain kinematic model as well as  $a_v$ ,  $a_d$ ,  $w_v$  and  $w_d$  within the logarithmic kinematic model, are obtained as the result of PFA calibration with the MD simulations (Levitas et al. (2017a, b)). In particular, Si I  $\leftrightarrow$  Si II transformation strain measures  $\varepsilon_t = (0.1753; 0.1753; -0.447)$  and  $\mathbf{H}(1) = \ln U_t(1) = (0.1616; 0.1615; -0.5924)$  are obtained using MD simulations. Therefore,  $J_t(1) = (1 + \varepsilon_{t1})^2 (1 + \varepsilon_{t3}) = 0.764$ ;  $\mathbf{trH} = \ln J_t(1) = -0.2694$ ;  $\mathbf{H}_{dd}(1) = \mathbf{devH} = (0.2513; 0.2513; -0.5026)$ .

#### 3.1. Trial calibration of the instability criteria

The lattice instability conditions for cubic-to-tetragonal Si I  $\leftrightarrow$  Si II PTs were obtained via MD simulations for various combinations of all six components of the Cauchy stress tensor in Levitas et al. (2017a, b). In 3D stress  $\sigma_i$  space, all points for direct and reverse instability stresses have been located close to two intersecting planes:

$$\begin{aligned} P_0 \rightarrow P_1: & \begin{cases} 0.36(\sigma_1 + \sigma_2) - \sigma_3 \geq 12.29 \text{ GPa} & \text{if } -\sigma_3 \geq 6.23 \text{ GPa} \\ 0.19(\sigma_1 + \sigma_2) - \sigma_3 \geq 9.45 \text{ GPa} & \text{otherwise} \end{cases} \\ P_1 \rightarrow P_0: & 0.19(\sigma_1 + \sigma_2) - \sigma_3 \leq 9.45 \text{ GPa}, \end{aligned} \quad (34)$$

For equal stresses in two lateral directions ( $\sigma_1 = \sigma_2$ ), the instability conditions are shown in 2D stress planes in Fig. 1.

It was obtained in Levitas et al. (2017a, b) that the contributions of shear stresses were negligible. It can be observed that increasing the lateral tensile stresses reduces not only the direct and reverse instability stresses but also their difference, namely the stress hysteresis, all the way down to the intersection point. From there on, the two instability lines coincide and the stress hysteresis vanishes. By equaling the PFA instability criteria for the transformation strain kinematic model, Eq. (31), with the MD lattice instability conditions, Eq. (34), the following equations are obtained

$$\begin{aligned} \left. \frac{a_{\varepsilon 1}}{a_{\varepsilon 3}} \left( \frac{\varepsilon_{t1}}{\varepsilon_{t3}} \right) \right. &= 0.36 \Rightarrow \frac{a_{\varepsilon 1}}{a_{\varepsilon 3}} = 0.9211 \quad \text{if } -\sigma_3 \geq 6.23 \text{ GPa} \\ \left. \frac{a_{\varepsilon 1}}{a_{\varepsilon 3}} \left( \frac{\varepsilon_{t1}}{\varepsilon_{t3}} \right) \right. &= 0.19 \Rightarrow \frac{a_{\varepsilon 1}}{a_{\varepsilon 3}} = 0.4896; \quad \text{otherwise} \end{aligned} \quad (35)$$

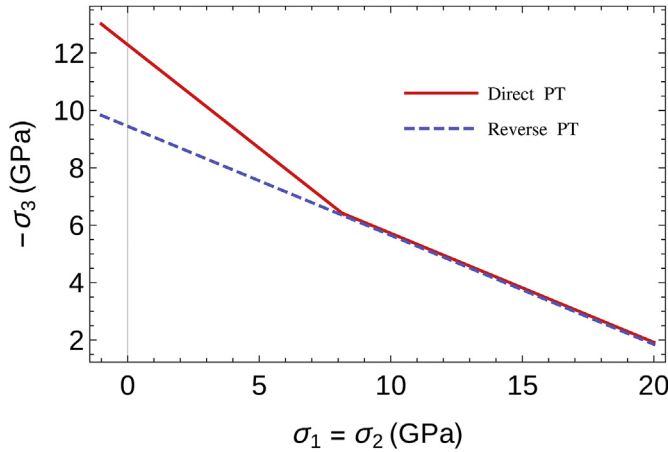


**Fig. 1.** Crystal lattice instability stress lines in 2D stress space for direct and reverse phase transformations in Si.  $\sigma_3$  is uniaxial compressive stress and  $\sigma_1 = \sigma_2$  are lateral biaxial tensile stresses.

$$\frac{w_{\varepsilon 1}}{w_{\varepsilon 3}} \left( \frac{\varepsilon_{t1}(1 + \varepsilon_{t3})}{\varepsilon_{t3}(1 + \varepsilon_{t1})} \right) = 0.19 \Rightarrow \frac{w_{\varepsilon 1}}{w_{\varepsilon 3}} = 1.0406; \quad (36)$$

$$\begin{cases} \frac{1}{J_e \varepsilon_{t3} a_{\varepsilon 3}} (A + 3\Delta\psi^\beta) = 12.29; & \text{if } -\sigma_3 \geq 6.23 \text{ GPa} \\ \frac{1}{J_e \varepsilon_{t3} a_{\varepsilon 3}} (A + 3\Delta\psi^\beta) = 9.45 & \text{otherwise}; \end{cases} \quad (37)$$

$$\frac{1 + \varepsilon_{t3}}{J_e \varepsilon_{t3} w_{\varepsilon 3}} (A - 3\Delta\psi^\beta) = 9.45, \quad (38)$$

which can be used to calibrate the four interpolation constants  $a_{\varepsilon 1}$ ,  $a_{\varepsilon 3}$ ,  $w_{\varepsilon 1}$  and  $w_{\varepsilon 3}$ . Furthermore, in the case of the logarithmic transformation strain-based kinematic model, by equaling Eq. (32) with Eq. (34) we obtain

$$\begin{cases} \frac{0.2513 - 0.0898 a_v / a_d}{0.5026 + 0.0898 a_v / a_d} = 0.36 \Rightarrow \frac{a_v}{a_d} = 0.5707 & \text{if } -\sigma_3 \geq 6.23 \text{ GPa} \\ \frac{0.2513 - 0.0898 a_v / a_d}{0.5026 + 0.0898 a_v / a_d} = 0.19 \Rightarrow \frac{a_v}{a_d} = 1.4462; & \text{otherwise} \end{cases} \quad (39)$$

$$\frac{0.2513 - 0.0898 w_v / w_d}{0.5026 + 0.0898 w_v / w_d} = 0.19 \Rightarrow \frac{w_v}{w_d} = 1.4462; \quad (40)$$

$$\begin{cases} \frac{1}{J_e a_d (0.5026 + 0.0898 a_v / a_d)} (A + 3\Delta\psi^\beta) = 12.29; & \text{if } -\sigma_3 \geq 6.23 \text{ GPa} \\ \frac{1}{J_e a_d (0.5026 + 0.0898 a_v / a_d)} (A + 3\Delta\psi^\beta) = 9.45 & \text{otherwise}; \end{cases} \quad (41)$$

$$\frac{1}{J_w_d (0.5026 + 0.0898 w_v / w_d)} (A - 3\Delta\psi^\beta) = 9.45, \quad (42)$$

which can be used to calibrate the constants  $a_v$ ,  $a_d$ ,  $w_v$  and  $w_d$ .

### 3.2. Stress-order parameter curve for the transformation strain-based interpolation function

However, a serious issue arises during the first attempt to calibrate parameters. The equilibrium stress-order parameter curve can be obtained by finding the third nontrivial root of the thermodynamic equation  $X(\sigma, \theta, \eta) = 0$  (i.e. excluding roots  $\eta = 0$  and  $\eta = 1$ ) and resolving it for stresses. Considering  $\sigma_1 = \sigma_2 = 0$  for brevity, we obtain the following for the transformation strain-based model

$$\sigma_3 = -\frac{(A(2\eta - 6\eta^2 + 4\eta^3) + \Delta\psi^\beta(6\eta - 6\eta^2))(1 + \varepsilon_{t3}\phi_3(\eta))}{J\varepsilon_{t3} \frac{d\phi_3(\eta)}{d\eta}}, \quad (43)$$

where

$$\phi_3(\eta) = a_{\varepsilon 3}\eta^2 + (10 - 3a_{\varepsilon 3} + w_{\varepsilon 3})\eta^3 + (3a_{\varepsilon 3} - 2w_{\varepsilon 3} - 15)\eta^4 + (6 - a_{\varepsilon 3} + w_{\varepsilon 3})\eta^5 \quad (44)$$

is the fifth-degree interpolation function for the third spatial direction. The plot of the function  $\sigma_3(\eta)$  is shown in Fig. 2a. The main problem is that this curve has a local minimum in  $0 < \eta < 1$  with the stress far below the instability stress for the reverse PT. With the fifth- and higher-degrees interpolation function  $\phi_3(\eta)$  for transformation strain, there is no way to eliminate this local minimum by

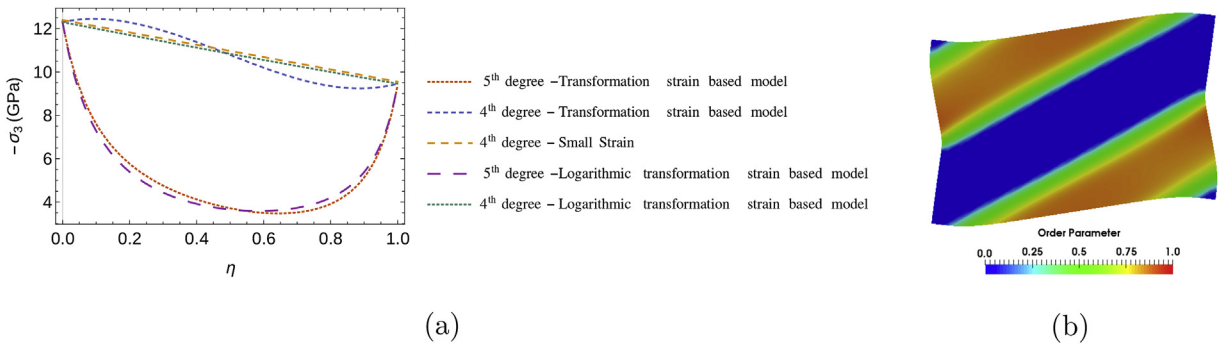


**Fig. 2.** (a) Equilibrium analytical Cauchy stress-order parameter curves for both kinematic models based on the transformation strain and logarithmic transformation strain, considering fourth-degree and fifth-degree interpolation functions. (b) Unphysical stationary nanostructure due to the fifth-degree interpolation function with local minimum in the stress-order parameter curve.

varying the material parameters  $a_{\varepsilon 3}$  and  $w_{\varepsilon 3}$ . Such a plot results in an unphysical stationary solution for the boundary-value problem, shown in Fig. 2b. The nanostructure in this figure is obtained for a thin square sample by applying compressive strain on the top and bottom faces with periodic boundary conditions and free lateral faces (see detailed problem formulation in Section 4). It can be seen that the solution forms partially-transformed bands with the value of the order parameter around 0.7 corresponding to the local minimum rather than 1.

To eliminate the undesired local minimum and obtain a monotonous stress-order parameter curve in the instability range, the interpolation polynomial for the third direction is reduced to a fourth-degree function by assuming  $w_{\varepsilon 3} = a_{\varepsilon 3} - 6$ :

$$\phi_3(\eta) = a_{\varepsilon 3}\eta^2 + (4 - 2a_{\varepsilon 3})\eta^3 + (a_{\varepsilon 3} - 3)\eta^4, \quad (45)$$

while two others remain fifth-degree. After canceling the common  $\eta$  and  $(1 - \eta)$  factors in the numerator and denominator, the stress-order parameter curve for this case simplifies to

$$\sigma_3 = -\frac{(A(1 - 2\eta) + 3\Delta\psi^\theta)(1 + \varepsilon_{t3}[a_{\varepsilon 3}\eta^2 + (4 - 2a_{\varepsilon 3})\eta^3 + (a_{\varepsilon 3} - 3)\eta^4])}{J\varepsilon_{t3}(a_{\varepsilon 3} - 2(a_{\varepsilon 3} - 3)\eta)}. \quad (46)$$

If we neglect the geometric nonlinearities for small strain formulation, and consider  $a_{\varepsilon 3} = 3$  this equation reduces to

$$\sigma_3 = -\frac{A(1 - 2\eta) + 3\Delta\psi^\theta}{3\varepsilon_{t3}}, \quad (47)$$

which is a linear expression in the order parameter (Fig. 2a).

However, as shown in Fig. 2a, despite significant progress, the equilibrium stress-order parameter curve is still slightly non-monotonous due to the effect of the geometric nonlinearity produced by the term  $(1 + \varepsilon_{t3}\phi_3(\eta))$  in the numerator of Eq. (43).

### 3.3. Stress-order parameter curve for the logarithmic transformation strain-based interpolation function

Interestingly, it turns out that the logarithmic strain based kinematic model can resolve the problem with the non-monotonous stress-order parameter curve in the instability range due to the geometric nonlinearity. Through the same process as for Eq. (43), we find the equilibrium stress-order parameter curve for the logarithmic model to be

$$\sigma_3 = -\frac{(A(2\eta - 6\eta^2 + 4\eta^3) + \Delta\psi^\theta(6\eta - 6\eta^2))}{J\left(H_v(1)\frac{d\phi_v(\eta)}{d\eta} + H_{dd}^{33}(1)\frac{d\phi_{dd}(\eta)}{d\eta}\right)}, \quad (48)$$

where

$$\begin{aligned} \phi_v(\eta) &= a_v\eta^2 + (10 - 3a_v + w_v)\eta^3 + (3a_v - 2w_v - 15)\eta^4 + (6 - a_v + w_v)\eta^5; \\ \phi_{dd}(\eta) &= a_d\eta^2 + (10 - 3a_d + w_d)\eta^3 + (3a_d - 2w_d - 15)\eta^4 + (6 - a_d + w_d)\eta^5. \end{aligned} \quad (49)$$

It can be observed that with the logarithmic strain formulation, there is no geometric nonlinear term in the stress function, which can resolve the issue with the transformation strain-based formulation. However, because there are still fifth-degree polynomials in the denominator of Eq. (48), it again leads to a undesirable local minimum within  $0 < \eta < 1$ . The same approach, namely reducing the polynomials in the denominator of Eq. (48) to the fourth degree, can be taken to remedy this issue. Thus, we assume  $w_d = a_d - 6$ , so that not only does  $\phi_{dd}$  reduce to a fourth-degree function, but Eq. (39) and Eq. (40) lead to  $w_v = a_v - 6$  and  $\phi_v$  reduces to a fourth-degree function as well. Therefore, after canceling the common factors  $\eta$  and  $(1 - \eta)$  in the numerator and denominator, the simplified stress-order parameter relation is obtained as

$$\sigma_3 = -\frac{A(1-2\eta) + 3\Delta\psi^\theta}{JH_v(1)(a_v - 2(a_v - 3)\eta) + JH_{dd}^{33}(a_d - 2(a_d - 3)\eta)}. \quad (50)$$

For the calibrated values of  $a_v$  and  $a_d$ , the logarithmic kinematic model with the fourth-degree interpolation functions results in the linear monotonous instability curve even for large strains.

### 3.4. Final calibration of the models

Therefore, to calibrate the parameters, first using Eqs. (37) and (38), and the mentioned additional condition  $w_{\varepsilon 3} = a_{\varepsilon 3} - 6$ , we obtain  $a_{\varepsilon 3}$ ,  $w_{\varepsilon 3}$ , and  $A$  in terms of  $\Delta\psi^\theta$ . Next, we plot the  $\sigma_3$  as a function of order parameter for various  $\Delta\psi^\theta$ . Then we find the best  $\Delta\psi^\theta$  that leads to a monotonous  $\sigma_3$  within the range  $0 < \eta < 1$ . Then, having the best fit for  $\Delta\psi^\theta$ , the calibrated  $a_{\varepsilon 3}$ ,  $w_{\varepsilon 3}$  and  $A$  are obtained. Next, Eqs. (35) and (36) are used to find  $\mathbf{a}_{\varepsilon 1}$  and  $\mathbf{w}_{\varepsilon 1}$ . The following interpolation constants  $a_\varepsilon$  and  $w_\varepsilon$  for transformation strain, double-well barrier magnitude  $A$ , and jump in the thermal energy  $\Delta\psi^\theta$  are the final results of the calibration procedure. First, for the transformation strain-based model:

$$\begin{aligned} \text{if } -\sigma_3 \geq 6.23 \text{ GPa} \rightarrow \\ \Delta\psi^\theta = 6.35 \text{ GPa}, A = 0.75 \text{ GPa}, a_{\varepsilon 1} = 3.31, a_{\varepsilon 3} = 3.60, w_{\varepsilon 1} = -2.48, w_{\varepsilon 3} = -2.39, \\ \text{otherwise} \rightarrow \\ \Delta\psi^\theta = 6.35 \text{ GPa}, A = -9.48 \text{ GPa}, a_{\varepsilon 1} = 1.10, a_{\varepsilon 3} = 2.26, w_{\varepsilon 1} = -3.88, w_{\varepsilon 3} = -3.73. \end{aligned} \quad (51)$$

Second, a similar process for the logarithmic strain based model results in

$$\begin{aligned} \text{if } -\sigma_3 \geq 6.23 \text{ GPa} \rightarrow \\ \Delta\psi^\theta = 6.42 \text{ GPa}, A = 2.34 \text{ GPa}, a_v = 1.81, a_d = 3.17, w_v = -4.08, w_d = -2.82, \\ \text{otherwise} \rightarrow \\ \Delta\psi^\theta = 6.42 \text{ GPa}, A = -2.55 \text{ GPa}, a_v = 4.61, a_d = 3.18, w_v = -5.27, w_d = -3.64. \end{aligned} \quad (52)$$

The Jacobian determinants,  $J$  and  $J_e$  at  $\eta = 1$  have been considered to be 0.64 and 0.76 respectively, based on their magnitude in our PFA simulations of Si I $\rightarrow$ Si II PT. The material parameters here are slightly different from those in Levitas (2018b) because multiplication of Jacobian determinants in the thermal part of the free energy that produces interfacial stresses, is neglected.

While there is a jump in material parameters ( $A$ ,  $\Delta\psi^\theta$ , etc.) at stresses for which both instability lines coincide, these jumps are obtained from conditions that instability stresses are continuous but have jump in derivatives, (see Fig. 1). If both states coexist in the solution of the boundary-value problem, instability stresses are again continuous across the boundary despite the jump in material parameters.

### 3.5. Stress-strain curves: PFA versus MD

More precise results for the compressive stress-strain curves considering different lateral tensile stresses are shown in Fig. 3. The

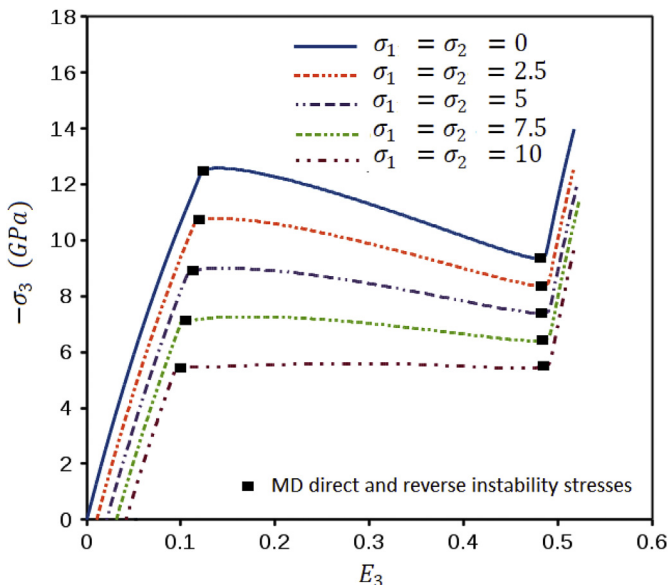


Fig. 3. True compressive stress,  $\sigma_3$ , versus Lagrangian strain,  $E_3$ , for different lateral tensile stresses, applied on a single element and obtained using PFA modeling; symbols are instability points obtained using the MD simulations (Levitas et al. (2017a)).

curves are obtained for a single finite element with homogeneous stress and strain using the transformation strain-based kinematic model. In this solution the Jacobian determinant is calculated rather than approximated. It can be observed that the instability points for both direct and reverse PTs, obtained with the PFA, are in satisfactory agreement with those of the MD simulations. Therefore, the calibration goal is achieved. Besides, the stress-strain curve is very slightly non-monotonous between instability points, causing a small increase in stresses at the beginning of direct PT. However, there is no local minimum of stresses before completion of the transformation.

#### 4. Effect of the lateral stress on nanostructure evolution: unusual phenomena

The FEM algorithm and numerical procedure have been developed in the deal.II program ([Bangerth et al. \(2007\)](#)), which is a C++ library aimed at the computational solution of partial differential equations. The three-dimensional and fully geometrically nonlinear response of an anisotropic crystal has been modeled. While the simulations are performed in the reference configuration, the results are presented in the deformed configuration.

A 3D square thin sample with the size of  $20 \times 20 \times 1 \text{ nm}^3$  is considered in this section. The periodic boundary condition for both solution variables, namely displacement and order parameter, is implemented on the top and bottom external pair faces (orthogonal to the axis 3). Also, the simulation box was subjected to a relative compressive displacement  $u_3$  between the upper and lower faces. The left and right lateral faces, as well as one of the faces in the thickness direction, were subjected to the homogeneous external tensile stresses  $\sigma_1 = \sigma_2$ . The other face in the thickness direction is fixed for normal-to-the-face displacement, namely  $u_2 = 0$ . One displacement degree of freedom in every direction is required to be fixed, which was done at the center of the sample. No shear stresses are applied to the external faces. Randomly distributed values within the range  $0 - 0.01$  are considered as the order parameter initial condition for all simulations.

The entire phase transformation process and nanostructure evolution is highly affected by the stress state. To study this effect, three different lateral tensile stress cases ( $\sigma_1 = \sigma_2 = 0, 5 \text{ and } 10 \text{ GPa}$ ) are considered. Macroscopic (averaged) stress-strain curves for all of the stress cases are plotted in [Fig. 4](#). For uniaxial compression at  $\sigma_1 = \sigma_2 = 0$ , the microstructure evolution is shown in [Fig. 5](#). It can be observed that once stress reaches the instability stress for direct PT, the order parameter starts to rise. Two martensitic bands, whose positions are governed by the periodic boundary conditions for the upper and lower external faces, are formed.

Initially, they consist of the intermediate structure; then transformation in bands completes and complete austenite-martensite finite-width interfaces are formed. The bands were initially slightly curved but they became planes after completion of the transformation within them. Transformation also started between bands but later it reversed back to the austenite. Such a microstructure with the optimal inclination angle minimizes the combined elastic and surface energies. The averaged stress  $\sigma_3$  drops during band formation and then remains practically constant during interface propagation, i.e. growth stage. When the interfaces start to overlap and the bands reach each other, the austenite disappears and stress drops again due to the disappearance of the interface and internal elastic energies.

For lateral stresses  $\sigma_1 = \sigma_2 = 5 \text{ GPa}$ , the evolution process still includes nucleation and band formation and propagation ([Fig. 6](#)). However, the band interfaces are widened and are not as plain and distinct as in the first case. Also, there are some regions of intermediate phase within the bands where PT is not completed. The stress-strain curve has the same features as in the case of  $\sigma_1 = \sigma_2 = 0$ , but, with smaller transformation stress and stress hysteresis, in accordance with [Fig. 4](#). This behavior can be qualitatively rationalized by considering the relationship between some parameters in the simplified model ([Levitas and Preston \(2002a\)](#)) for

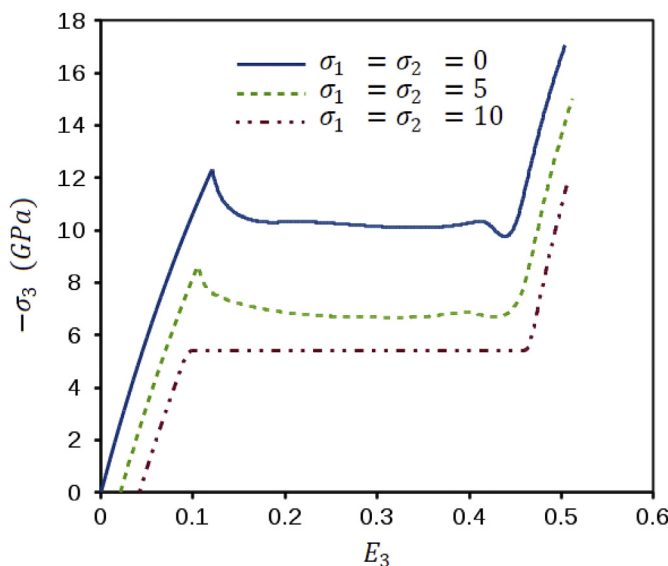


**Fig. 4.** True compressive stress,  $\sigma_3$ , versus Lagrangian strain,  $E_3$ , for three different lateral tensile stresses.

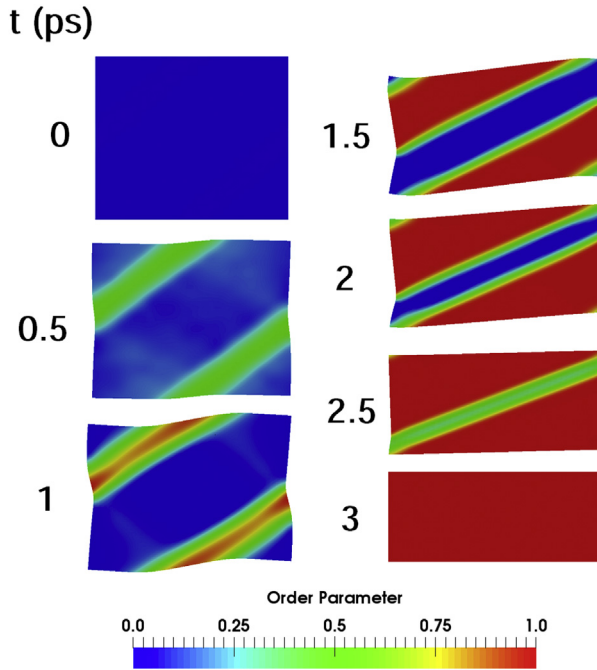


**Fig. 5.** Evolution of martensitic nanostructure in Si I - Si II PT for uniaxial compression under  $\sigma_1 = \sigma_2 = 0$ .

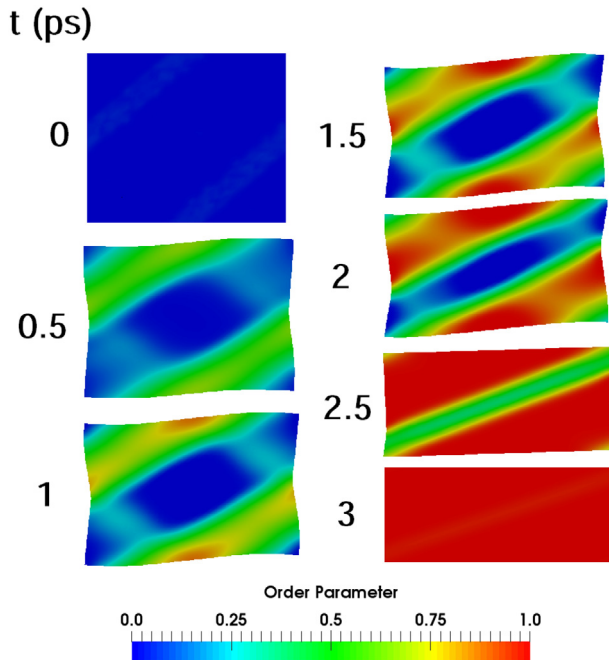


**Fig. 6.** Evolution of martensitic nanostructure during Si I - Si II PT under compression and tensile lateral stresses  $\sigma_1 = \sigma_2 = 5$  GPa.

which an analytical solution is available (Levitas et al. (2003)). Thus, for the uniaxial stress-strain curve, the stress hysteresis  $H$  during the PT is proportional to the magnitude of the double-well energy barrier between phases at equilibrium  $\tilde{A}$ . On the other hand, the interface energy  $\gamma \sim \sqrt{\tilde{A}}$  and interface width  $\delta \sim 1/\sqrt{\tilde{A}}$ . Therefore, reduction in stress hysteresis because of lateral tensions, not only reduces  $\tilde{A}$  and in turn the interface energy but also increases the interface width. As a result, the interface widths are comparable with the sample size, leading to various size effects (Levitas et al. (2006a, b)). When complete martensitic bands with plane interfaces are formed, the material between them is already in the intermediate state with  $\eta \approx 0.5$ .

The next case with the lateral stresses  $\sigma_1 = \sigma_2 = 10$  GPa (Fig. 7) corresponds to the merged region of the instability lines where the

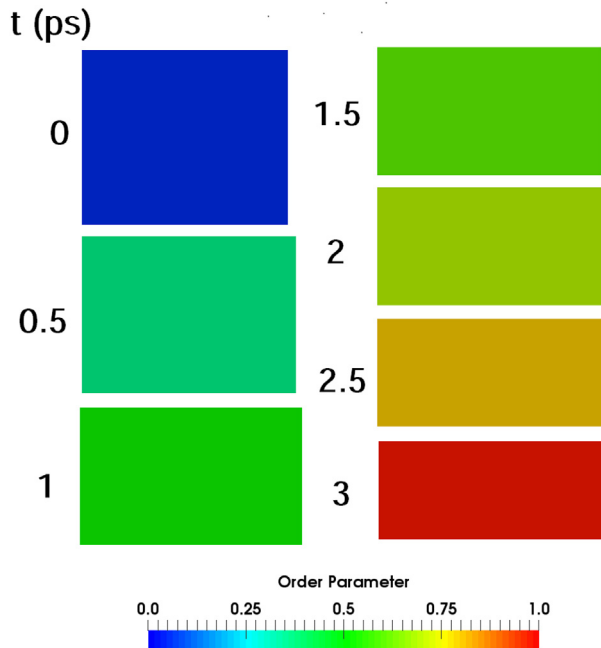


**Fig. 7.** Evolution of martensitic nanostructure in Si I - Si II PT under compression and tensile lateral stresses  $\sigma_1 = \sigma_2 = 10$  GPa: unique homogeneous phase transformation.

stress hysteresis disappears. As shown in Fig. 7, despite considering a heterogeneous initial perturbation for the order parameter, the system undergoes a unique homogeneous and hysteresis-free first order PT with no nucleation and two-phase band formation and growth. The same behavior was observed in MD simulations for Si I $\rightarrow$ Si II PTs for such stress states at which the instability lines for direct and reverse PTs coincide (Levitas et al. (2017a)). To give a simple geometric and energetic interpretation of this phenomenon, we consider small strains and will operate with the Gibbs energy per unit volume for homogeneous states  $G(\sigma, \eta, \theta) = \psi(\varepsilon, \eta, \theta) - \sigma : \varepsilon$ , the same as what was done in Levitas and Preston (2002a). Formulation of the Gibbs energy in terms of the Cauchy stress for large strains encounters major problems due to the lack of a strain measure which is work-conjugate to the Cauchy stress for the general loading. However, small strain interpretation of Gibbs energy is sufficient for our purposes. For the fixed stress tensor and temperature and equal energy of the phases, a schematic plot of the Gibbs energy versus order parameter is shown in Fig. 8. With increasing tensile lateral stresses,

$$H \sim \tilde{A} \rightarrow 0 \Rightarrow \delta \sim 1/\sqrt{\tilde{A}} \rightarrow \infty \quad \& \quad \gamma \sim \sqrt{\tilde{A}} \rightarrow 0, \quad (53)$$

i.e. the stress hysteresis and energy barrier  $\tilde{A}$  between phases tend to zero resulting in a flat (plateau) region in the Gibbs energy, diverged interface width and zero interface energy. With the barrier, there are two reasons for PTs through nucleation and growth

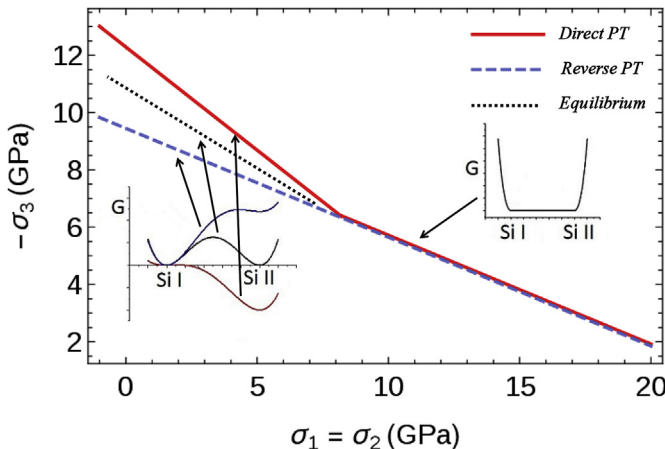


**Fig. 8.** Schematics of the Gibbs energy curves for different stress states at direct and reverse instability lines.

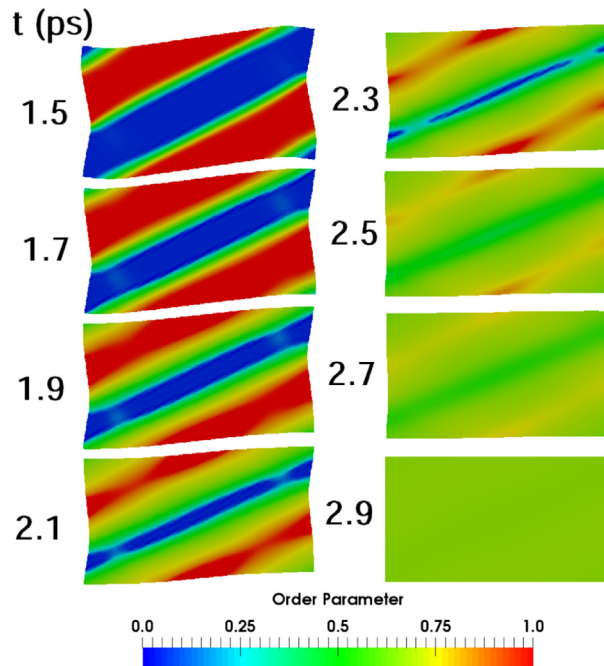


**Fig. 9.** Nanostructure evolution during transformation of the two-phase Si I-Si II mixture into the intermediate homogeneous phase with the order parameter  $\eta = 0.66$  under fixed strain  $E_3 = 0.3$  and increasing tensile lateral stresses from 0 to 10 GPa.

within a two-phase structure. First, thermally activated or heterogeneous barrierless nucleation may occur only in a small volume. Second, the energy of a two-phase mixture is smaller than the energy of homogeneous intermediate states. Without the barrier, there is no need for nucleation in the small volume and because the interface width is infinite, it is larger than any finite-size sample. This is why the entire system homogeneously transforms while passing through the intermediate states (phases), which all have the same Gibbs energy and, consequently, are in indifferent thermodynamic equilibrium with the product and parent phases. Each of the infinite number (i.e. continuum) of intermediate states can be considered as a separate phase with a distinct lattice parameter, and transformation between each of them is accompanied by a change in the strain and the latent heat. Each intermediate phase can be arrested by fixing one of the strain components and studied in a bulk sample. They may possess unique and desirable material properties; in particular, electronic transition from semiconducting to metallic phase occurs along this path. In addition, coherent interfaces between phases generate elastic stresses which lead to accumulated damage during cyclic direct and reverse PTs. For homogeneous PT, internal stresses are absent and damage should be minimal.

To summarize, PFA, similar to MD, predicts that it is possible to find special stress states for which unique homogeneous, hysteresis-free, dissipation-free, and damage-free direct and reverse PTs can occur through a continuum of intermediate phases in indifferent thermodynamic equilibrium transition. All of these properties are the optimal ones for multiple PT-related applications (Cui et al. (2006)), such as shape memory and elastocaloric applications. Moreover, they are also of great fundamental interest.

Finally, transition from a two-phase intermediate structure to a homogeneous intermediate structure is studied. Therefore, a uniaxial compressive strain  $E_3 = 0.3$  at  $\sigma_1 = \sigma_2 = 0$  is applied to the sample to obtain complete martensitic bands and an intermediate two-phase state, the same as in Fig. 4. Afterwards, further straining is stopped; namely  $E_3$  remains constant, and lateral tensile stress is applied gradually up to  $\sigma_1 = \sigma_2 = 10$  GPa, i.e. up to the state with no stress hysteresis and energy barrier between phases. It can be observed in Fig. 9 that by approaching the stress state with merged region of instability lines, the interface width in the traditional two-phase system increases and the order parameter decreases from 1 to some intermediate value. At  $t > 2.3$ , Si I disappears and the sample consists of a heterogeneous intermediate structure which does not contain Si I and II. At  $t = 2.9$ , the system completes its gradual transformation to the intermediate homogeneous phase. Again, all of the unique heterogeneous intermediate structures that the system goes through and which may possess unexpected properties, can be stabilized and studied. As shown in Fig. 10, the stress  $\sigma_3$  drops to the instability stress corresponding to the applied lateral stress at constant  $E_3$ .

For comparison, the same problem as in Fig. 5 (i.e. for the same boundary condition, material parameters and loading condition) was solved for the logarithmic transformation strain-based model. The nanostructures in Fig. 11, significantly differ from those in Fig. 5. Curved incomplete martensitic bands with widened interfaces and internal heterogeneous structures are observed, and transform to nearly straight bands with intermediate structure and then to Si II. We hypothesize that the difference is caused by much larger elastic interfacial stresses for this model in comparison with the model based on the interpolation of the transformation deformation gradient. This model was obtained in Basak and Levitas (2017) for a twin interface that the elastic interfacial stress for the logarithmic model is more than two times larger than for the transformation deformation gradient based model. To reduce the additional elastic interfacial energy, the system increases the interface width and produces intermediate phases. Therefore, although

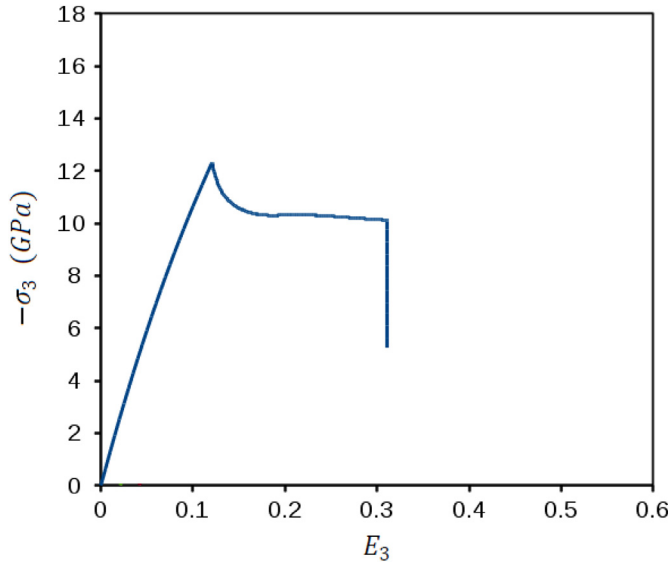


**Fig. 10.** True compressive stress,  $\sigma_3$ , versus Lagrangian strain,  $E_3$ , for the loading and nanostructure evolution shown in Fig. 8. Note that the PFA results obtained in this section are in good qualitative agreement with the MD results in Levitas et al. (2017a, b). Homogeneous PT is not related to the small size (Levitas et al. (2006a, b)) but is a consequence of zero energy barrier between phases. In MD simulations Levitas et al. (2017a, b), the same results were obtained when sample size varied from 5 to 40 nm. For small hysteresis, when the increased interface width is becoming comparable with the sample size or the distance between martensitic bands, the microstructure is also affected by the sample size.

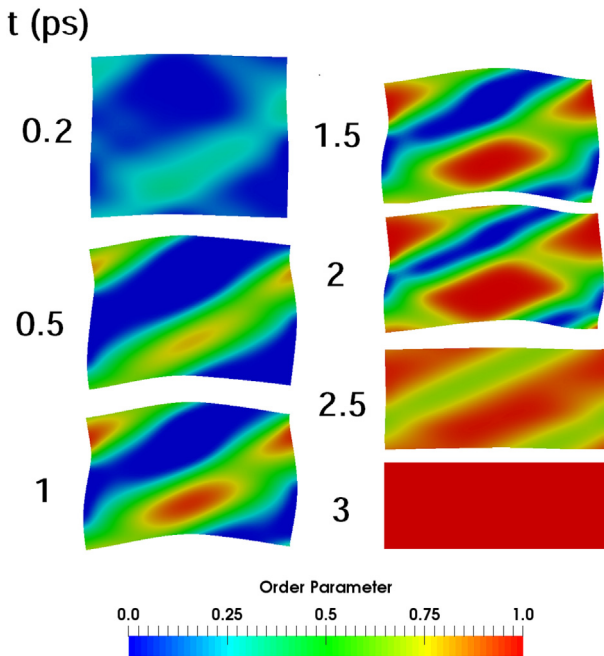


**Fig. 11.** Evolution of martensitic nanostructure during Si I - Si II PT for uniaxial compression under  $\sigma_1 = \sigma_2 = 0$  and the logarithmic strain based interpolation.

the logarithmic transformation strain-based model is highly beneficial due to separation of the effect of change in volume and shape and corresponding terms in the driving force for PT and instability conditions, as well as because of the monotonous stress-order parameter curve for finite strains, one must find a way to reduce the elastic interfacial stresses before it can be used for nanostructure modeling. For this reason, the transformation strain-based model will be used for the rest of the simulations in this study.

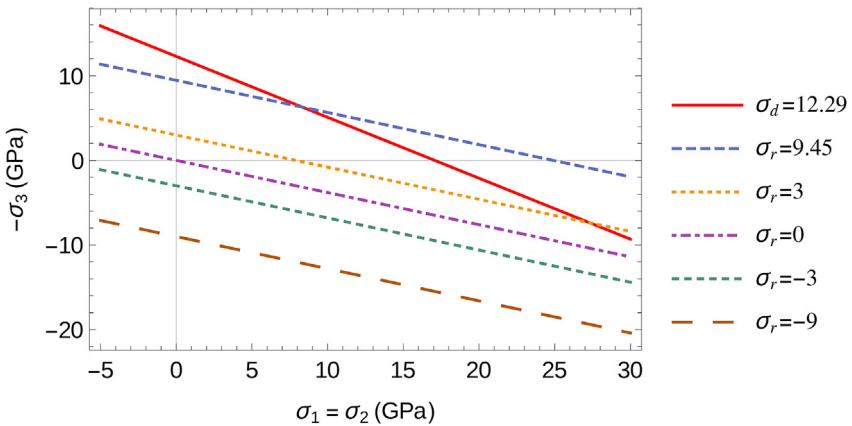


**Fig. 12.** Instability line for the direct PT and five different instability lines for the reverse PT used in studying the effect of stress hysteresis on the nanostructure evolution.

### 5. Effect of the stress hysteresis on the nanostructure evolution

In this section, we perform simulations for a cubic sample of size  $20 \times 20 \times 20 \text{ nm}^3$  and periodic conditions on all external pair faces for the model with the transformation strain-based interpolation. We apply compressive displacements  $u_3$  to the upper face of the box with respect to the lower face along the vertical axis. Tensile relative displacements  $u_1 = u_2 = 0.28u_3$  were applied to the box on both lateral faces, where 0.28 was the factor determined numerically for uniaxial loading of Si I before PT. A single point at the center of the cube is fixed for displacement in all directions. No shear stresses are applied to the external faces. We expect that, for such a sample, the internal stresses will be much larger than in the previous thin plate domain, which may lead to some interesting effects. The magnitude of the stress hysteresis effect on the nanostructure evolution has been studied based on the result. All cases of the instability lines are shown in Fig. 12. These lines are characterized by the instability stress at  $\sigma_1 = \sigma_2 = 0$ . We keep the same instability line for the direct PT ( $\sigma_d = 12.29$  GPa) and consider five parallel lines for the reverse PT from  $\sigma_r = 9.45$  GPa, obtained from

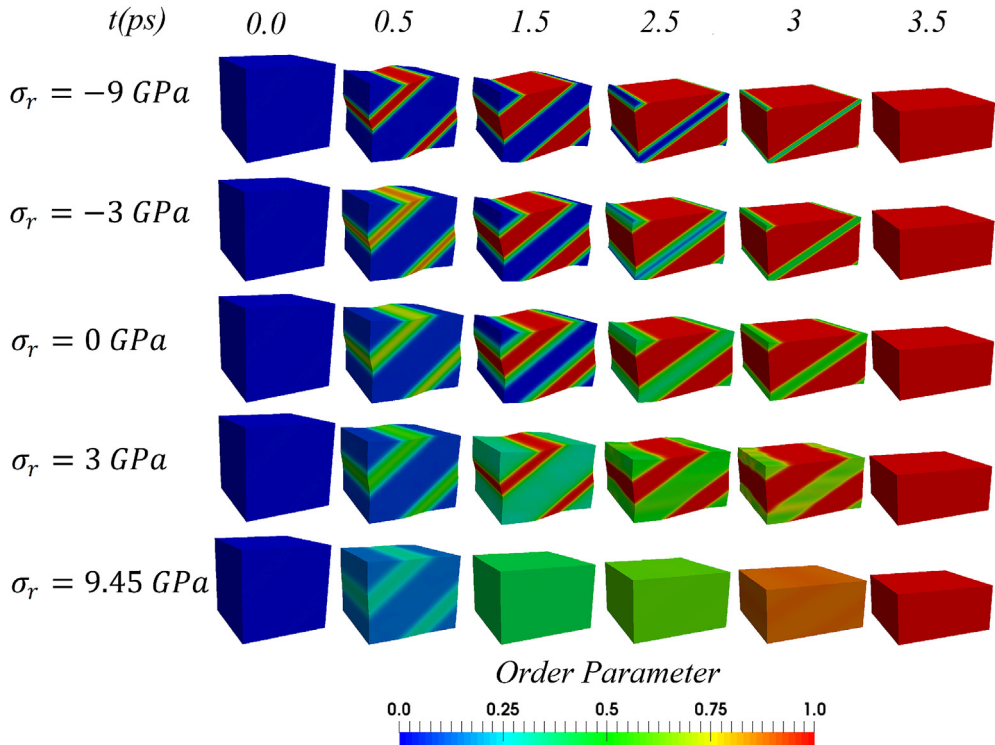


**Fig. 13.** Nanostructure evolution corresponding to five different instability stresses for the reverse PT under uniaxial compression, with periodic boundary conditions on all pair faces.

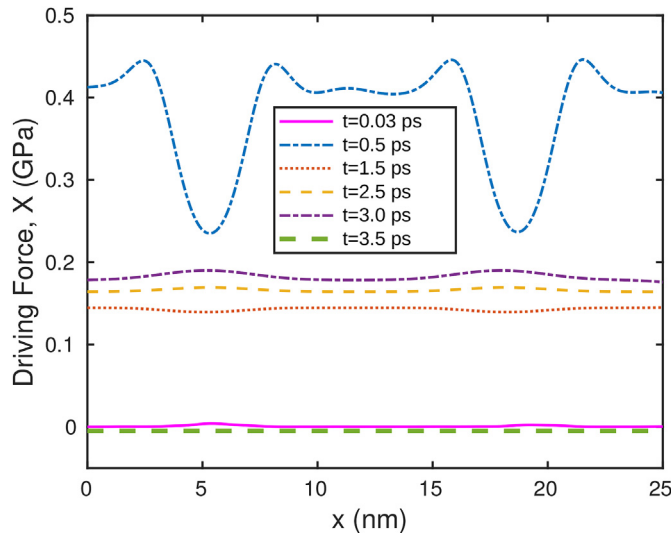


**Fig. 14.** Thermodynamic driving force along a line passing through the nanostructure from the upper left corner to the lower right corner for the case  $\sigma_r = 9.45$  GPa.

the MD calibration, down to  $\sigma_d = -9$  GPa for comparison. The evolutions of the nanostructure for all cases are shown in Fig. 13. To analyze the difference in the nanostructure evolution for different cases, the total driving force for PT,  $X$ , is plotted along a line passing through the sample connecting the upper left corner to the lower right corner in Figs. 14–16 for different  $\sigma_r$  cases. Surprisingly, for  $\sigma_r = 9.45$  GPa with the lowest hysteresis, evolution of the order parameter starts everywhere with the appearance of two incomplete bands, which continuously transform to the intermediate homogeneous structure and undergo a homogeneous transformation afterwards. As shown in Fig. 14, at  $t = 0.5\text{ps}$ , the driving force outside of the initial intermediate bands exceeds the driving force within the bands, leads to the disappearance of the initial tendency to form martensitic bands, and transforms the system transition to a homogeneous PT with uniform driving force across the domain. For  $\sigma_r = 3$  GPa and a broader hysteresis, the first transformation starts within two bands with maximum driving force within them. However, as shown in Fig. 15, there is considerable driving force outside the martensitic bands. Thus, along with the completion of the transformation in the martensitic bands, the austenite becomes unstable outside the martensitic bands and starts transformation as well. Further evolution combines the broadening of the of martensitic bands and an increase in the order parameter between them. Regarding the case  $\sigma_r = 0$  GPa, with even broader hysteresis, when transformation was completed within two martensitic bands, two wide complete austenite-martensite interfaces were formed, as would be expected. However, due to the relatively large widths of the interfaces, they overlap and a significant part of the sample transforms through the increase in the order parameter between the growing martensitic bands. For lower  $\sigma_r$ , namely  $\sigma_r = -3$  and  $\sigma_r = -9$ , the interface width is smaller and PT occurs in a traditional way through formation and growth

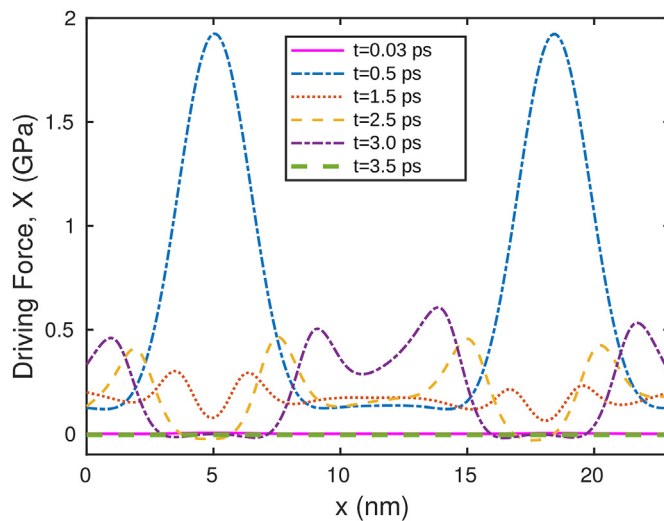


**Fig. 15.** Thermodynamic driving force along a line passing through the nanostructure from the upper left corner to the lower right corner for the case  $\sigma_r = 3$  GPa.

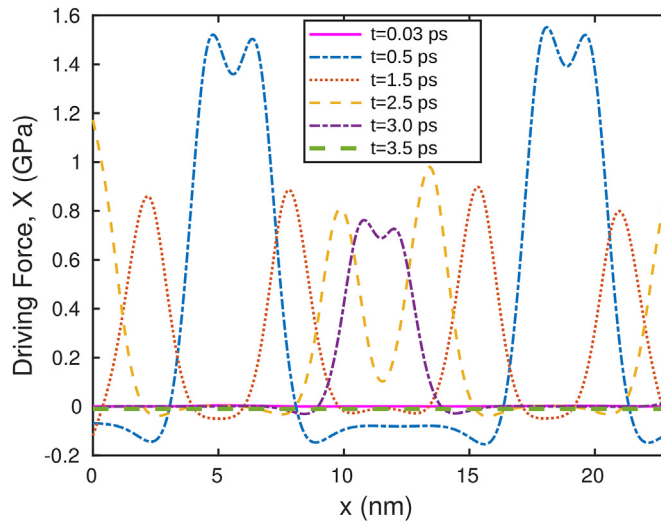


**Fig. 16.** Thermodynamic driving force along a line passing through the nanostructure from the upper left corner to the lower right corner for the case  $\sigma_r = -3$  GPa.

of two fully transformed bands. As  $\sigma_r$  decreases, the interface width decreases as well so that the case  $\sigma_r = -9$  has the thinnest interface. It can be observed in Fig. 16 that the driving force is always at its maximum at the interface and negative in the austenitic regions.

Two factors are responsible for the observed phenomena. First, with the reduction of the stress hysteresis, the widths of all interfaces increase and the total width of all interfaces becomes comparable with the sample height, which decreases during PT. As a result, the interfaces overlap and produce the transformation everywhere in a sample, in addition to broadening of the martensitic plate. Second, internal stresses are much larger for the 3D cube sample than for the thin sample, especially  $\sigma_2$  in the direction orthogonal to the front face of the cube. They are tensile in the austenite and compressive in the martensite. Thus,

- (a) they suppress the evolution of the order parameter with incomplete martensitic bands,
- (b) promote the transformation within austenite and regions with smaller order parameters rather than in the main martensitic bands, and
- (c) reduce the stress hysteresis and increase the interface width in the intermediate region with tensile stresses.

Therefore, due to these effects, one observes the entire spectrum of the above phenomena depending on  $\sigma_r$  and the hysteresis width.

## 6. Stress field within the interface

Regarding the problem with  $\sigma_r = -3$  GPa, the evolution of normal stress fields in three mutually orthogonal directions including normal to the front face stress,  $\sigma_2$ , normal-to-the-interface stress,  $\sigma_n$ , and tangential-to-the-interface stress,  $\sigma_t$ , are shown in Fig. 17 in 3D and in Figs. 18–20 along a line connecting two points at the center of the martensitic bands. By comparing three stress fields, it can be observed that  $\sigma_2$  has the largest variation between the austenitic and martensitic regions. Such a large difference in  $\sigma_2$  comes from the transformation expansion of  $\epsilon_{12} = 0.1753$  within the martensitic bands, which generates a tensile stress in the austenite and a compressive stress in the martensite. Stress  $\sigma_2$  varies monotonously inside the diffuse interface. Once the martensitic band is completed, the stress  $\sigma_2$  in the martensite reaches  $-14$  GPa and remains constant for some steps. Also, during the band propagation, the stress in the austenite grows from 3 to 10 GPa due to the widening of the martensitic bands. As the martensitic bands approach each other, their interfaces overlap and mismatch reduces, which in turn results in a drastic reduction of the internal stresses. The stress in the martensite reduces to  $-15.5$  GPa, and because the difference between the stresses in the martensite and the overlapped interface region drastically decreases, the stress  $\sigma_2$  in this region falls from 10 GPa to  $-15.5$  GPa. Finally, when the martensitic bands coalesce,  $\sigma_2$  is homogeneous and the magnitude of the compressive stress slightly increases due to the loading.

The internal stresses  $\sigma_t$  are much smaller than  $\sigma_2$ , because the lattice mismatch in this direction is significantly reduced due to optimal inclination of the interface, theoretically to zero. This is governed by minimization of the elastic energy of the internal stresses. Thus, the difference between the stresses in the austenite and the martensite decreases from 2 GPa to zero. Interestingly, the internal stresses, when nonzero, are compressive in the austenite and tensile in the martensite. They increase slightly when the interfaces start overlapping and then monotonously reduce to zero during coalescence of the two plates. The magnitude of the compressive  $\sigma_t$  stress then increases homogeneously due to loading.

An important problem is the definition of the interfacial tension (stresses). Any interfacial property is defined as an integral along

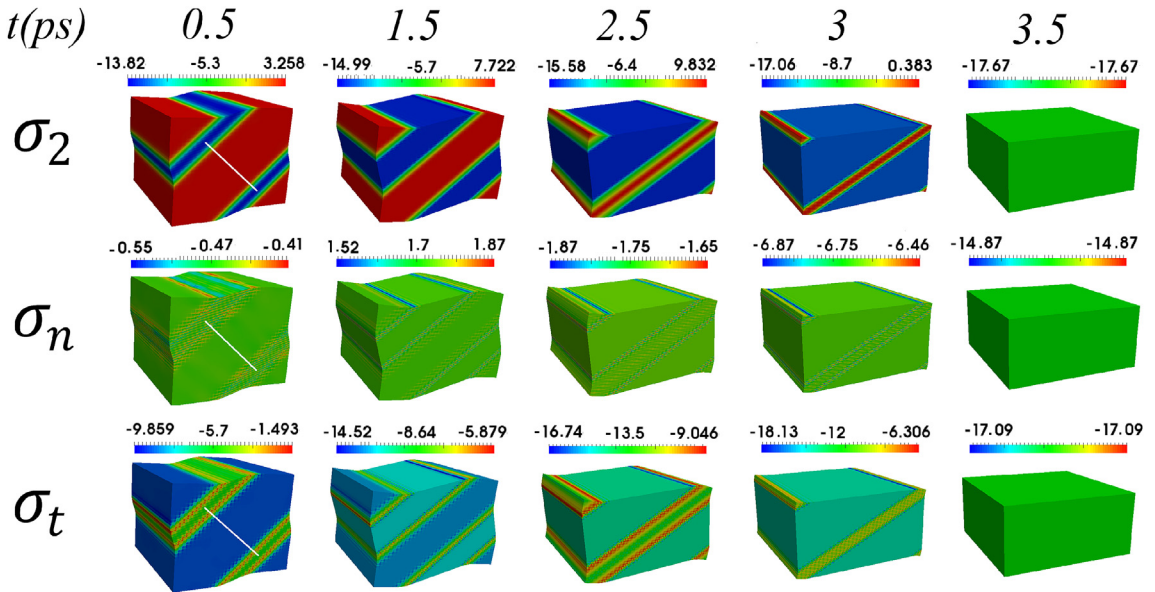


**Fig. 17.** Evolution of normal stress fields in three mutually orthogonal directions including normal-to-the-front-face stress,  $\sigma_2$ , normal-to-the-interface stress,  $\sigma_n$ , and tangential-to-the-interface stress,  $\sigma_t$ , for the problem with  $\sigma_r = -3$  GPa.

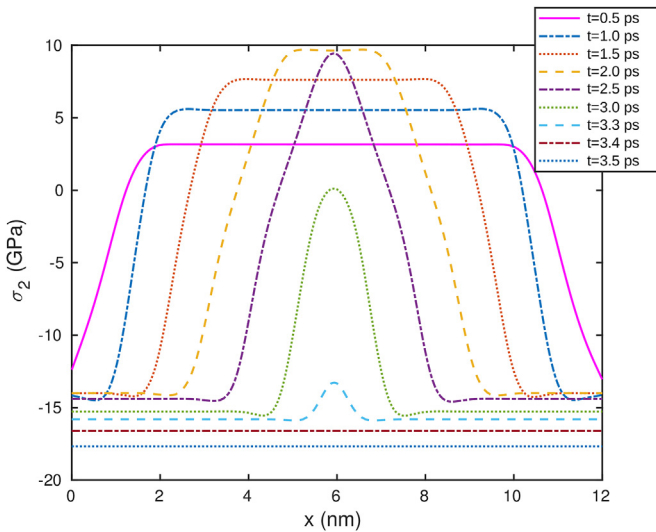


**Fig. 18.** Evolution of  $\sigma_2$  for the solution shown in Fig. 16 along a line passing through the austenitic and martensitic bands shown in Fig. 16.

the interface normal of the excess quantity within the interface with respect to the bulk value (Gibbs (1948); Fischer et al. (2008); Sutton and Balluffi (1995)). It is straightforward to define excess stress  $\sigma_l$  for  $t \geq 2\text{ps}$ , when values of the stress  $\sigma_l$  in bulk from both sides of a single interface or merged interfaces are the same. These values vary from  $4.33 \text{ J/m}^2$  for  $t = 2\text{ps}$  to  $8.54 \text{ J/m}^2$  for  $t = 3\text{ps}$ . For instance, when there is a difference between the values of stresses from both sides of the interface, for instance, at  $t = 1.5\text{ps}$  for  $\sigma_l$ , one must choose a dividing surface and integrate an excess of  $\sigma_l$  with respect to the value in the martensite from the martensite side to the dividing surface and with respect to the value in the austenite from the austenite side to the dividing surface. The position of the dividing surface is strictly defined only for the liquid-gas and liquid-liquid interfaces, which do not support bending moments (Levitas (2014b, a)). One can use the zero-moment condition for determining the position of the dividing surface for solids as well, which means that the distributed stresses are substituted with the resultant force without moments. When the difference in stresses in bulk from both sides of the interface are small, a small deviation in the position of the dividing surface does not change the surface tension significantly. However, for monotonous variation within the interface stresses  $\sigma_2$  (Fig. 18), the resultant force strongly depends on the choice of the dividing surface and there is a large bending moment for any position of the dividing surface within an interface. Thus, a strict definition of the interfacial force and the bending moment for interfaces in solids is an open problem.

The stress  $\sigma_n$  is constant within the sample, i.e. it is continuous across each of the interfaces, in agreement with mechanical

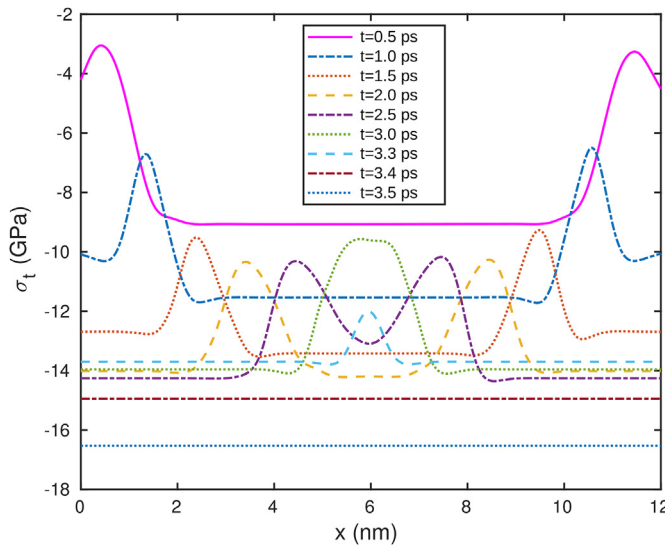


Fig. 19. Evolution of  $\sigma_t$  for the solution shown in Fig. 16 along a line passing through the bands.

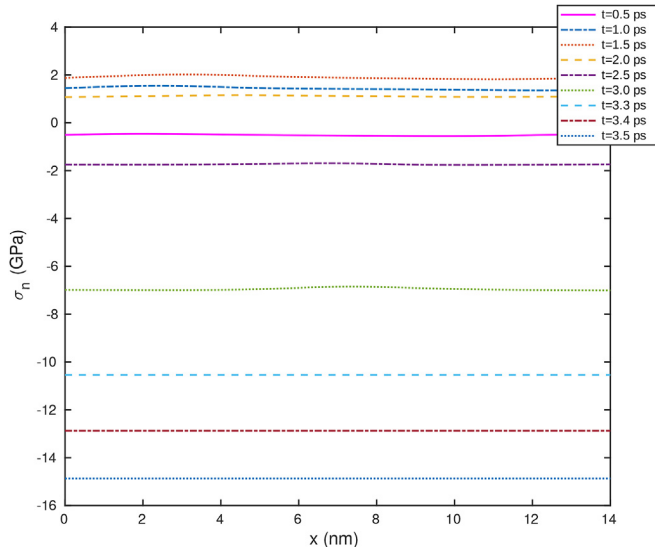


Fig. 20. Evolution of  $\sigma_n$  for the solution shown in Fig. 16 along a line passing through the bands.

equilibrium in the normal-to-the-interface direction (Fig. 20).

Note that the difference in stresses in coexisting Ge I and Ge II under pressure during Ge I $\rightarrow$ Ge II PT (very similar to the Si I $\rightarrow$ Si II PT) was recently measured with in situ synchrotron x-ray diffraction and Raman spectroscopy (Yan et al. (2015)).

## 7. Concerning the independence of instability condition of the prescribed stress tensor

It is well-known and intuitively understood that any instability condition under large strains depends on which stress measure is prescribed (Hill and Milstein (1977); Milstein et al. (1995); Wang et al. (1993)). On the other hand, it was strictly proven for our PFA that the lattice instability criterion is independent of the prescribed stress measure (Levitas (2013, 2018b)). This independence is a consequence of the accepted requirement that the order parameters for austenite ( $\eta = 0$ ) and martensite ( $\eta = 1$ ) satisfy the condition  $X = 0$  for all stresses and temperatures. Such a difference with well accepted results requires further analyses.

Although the independence of the lattice instability condition of the prescribed stress measure can be strictly analytically proven, here it is investigated numerically for prescribed Cauchy and first Piola-Kirchhoff stresses. We consider a single 3D finite element with homogeneous stress and strain and stress-free lateral faces. First, through a uniaxial strain-controlled compressive loading in the vertical direction, the stress-strain curves for both the Cauchy and the first Piola-Kirchhoff stresses are obtained, as shown in Fig. 21. According to the definition, our instability condition is concerned with a deviation of the order parameter from zero. It can be

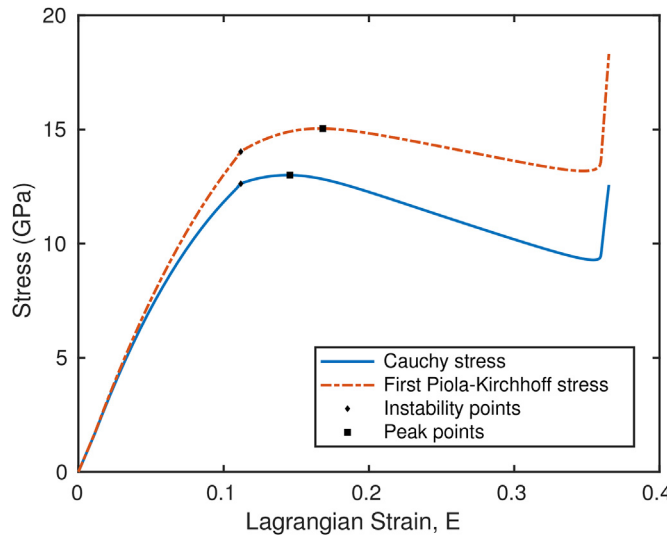


**Fig. 21.** Stress-strain curve for uniaxial compressive strain-controlled loading for both the Cauchy and first Piola-Kirchhoff stresses. Markers show corresponding instability points and stress peak points.

observed that such an instability at which the driving force for the change of the order parameter,  $X$ , becomes positive and the order parameter starts to rise, occurs at a specific strain marked in Fig. 21, and the corresponding Cauchy and the first Piola-Kirchhoff instability stresses are obtained.

Now let us consider two different loadings with the prescribed Cauchy and the first Piola-Kirchhoff stresses instead of displacement. In each case, once each of the stress measures exceeds the corresponding instability stress, the order parameter ceases to be zero and starts to rise. This means that, the instability condition is met and that the instability indeed starts at the same value of the strain corresponding to the values of the Cauchy or the first Piola-Kirchhoff stresses, independent of which stress is prescribed. However, such an instability does not mean that the order parameter will continue evolving to unity toward the completion of the PT with fixing stresses at the instability values. This is because the peak points, i.e. maximum stress points, do not coincide with the instability points and are located at strains larger than the instability strains. This means that if we prescribe the Cauchy or the first Piola-Kirchhoff stresses between the instability and the peak points for each of the curves, the instability occurs, however, the order parameter and strain are equilibrated at some values corresponding to the prescribed stresses. When the prescribed Cauchy stress slightly exceeds the corresponding peak point, a second instability occurs, the order parameter evolves to unity, and PT is completed. Even if the instability and peak stresses coincide for the Cauchy stress (like in small strain models), for the first Piola-Kirchhoff stress it may still not coincide and the second instability will depend on the prescribed stress measure.

Thus, the instability point for the deviation of the order parameter from zero is indeed independent of the prescribed stress measure. However, if the peak points do not coincide with the instability points, the stress for completion of the PT represents the second instability points, and they depend on the prescribed stress measure.

During the solution of a boundary-value problem with heterogeneous fields, stress tensors can only be prescribed at the boundaries and each material point within the bulk undergoes a sophisticated loading process. Therefore, defining which stress is prescribed at each point is impossible. Let us consider the case of a heterogeneous process in which the Cauchy stress exceeds the peak point but the first Piola-Kirchhoff stress does not, i.e. strain is between two peak points. Because one of the instability conditions (for the Cauchy stress) is met and there is no constraint that the instability condition for the first Piola-Kirchhoff stress should also be satisfied, PT may evolve until completion. This means that the fulfillment of the instability criterion for at least one of the stress measures (in the given case for the Cauchy stress) is sufficient for material instability. As a corroborating example, we mention that the curve for the second Piola-Kirchhoff stress versus the Lagrangian strain is monotonous through the PT (Levitas et al. (2017b)), i.e. there is no peak stress and no second instability point when the second Piola-Kirchhoff stress is prescribed. This, however, does not prevent PT in simulations when the second instability point for other stress measures is overcome.

Thus, the chief stress measure that is responsible for PT completion is the measure with the lowest strain at the peak point. Because of this, it is reasonable that the PT criterion for multiaxial compression in Levitas et al. (2017b) is formulated in terms of the Cauchy stress. It is worth mentioning that, for the PT caused by tension, the tensile Cauchy stress exceeds the first Piola-Kirchhoff stress and the latter is the chief stress measure that is responsible for the complete PT.

## 8. Concluding remarks

This two-part paper brings description of mechanically-induced PTs to a new level and makes it consistent with the results of MD simulations under multiaxial loading. A complete system of equations of the advanced PFA for martensitic PTs under a general stress tensor is presented. Theory includes a fully geometrically-nonlinear formulation for the general case of finite elastic and

transformational strains, as well as anisotropic and different elastic properties of phases. In particular, material parameters are calibrated based on the crystal lattice instability conditions obtained using MD simulations for cubic to tetragonal Si I $\leftrightarrow$ Si II PTs during compression in one direction and lateral tensile stresses in two other directions. These PTs fully test the general theory because they are characterized by large transformation strains,  $\varepsilon_t = (0.1753; 0.1753; -0.447)$ , and finite elastic strains. This allowed us to address several problems which do not exhibit themselves for smaller strains. Two large-strain kinematic models, one based on interpolation of the transformation strain tensor and the other on interpolation of the logarithmic transformation strain, are used. A FEM algorithm and numerical procedure was developed and implemented in the code deal.II. Various 3D problems on lattice instabilities and following nanostructure evolution in single-crystal silicon are solved and analyzed for complex loading in three cubic directions.

The key feature of the Si I $\leftrightarrow$ Si II PTs is that the instability lines for direct and reverse PTs have different slopes so that they intersect and then coincide, which follows from MD simulations (Levitas et al. (2017a, b)). Such a case was never considered within PFA before, and it has a number of important consequences.

- (a) Each independent component of the transformation strain tensor should have a different material parameter in the interpolation polynomial. Note that the interpolating function for transformation strain evolved from  $\eta$  (Salje (1990); Ichitsubo et al. (2000); Artemev et al. (2001)) and  $\eta^2$  (Lindgård and Mouritsen (1986); Boulbitch and Toledano (1998); Wang and Khachaturyan (1997); Artemev et al. (2000)) to one-parametric fourth-degree potential (Levitas and Preston (2002a, b); Levitas (2013)) and 2–4–6 potential (Levitas et al. (2003); Levitas (2013)) for the entire transformation strain tensor. Here, we developed a two-parametric fifth-degree polynomial with different parameters for each independent component of the transformation strain tensor.
- (b) The traditional fourth-degree interpolating polynomials (Levitas and Preston (2002a, b); Levitas (2013)) are not sufficient and thus the fifth-degree polynomials must be used. However, the general wisdom that one can resolve all current and future problems by increasing the degree of polynomials, failed. Thus, for the fifth-degree and higher-degree polynomials for each component of the transformation strain tensor, the stress-order parameter curve (and, consequently, the stress-strain curve) for uniaxial compression has unacceptable features. Namely, instead of monotonous reduction in stress from its value at  $\eta = 0$  to its value at  $\eta = 1$ , stress reaches a minimum value for some  $0 < \eta < 1$ , which is much lower than the stress at  $\eta = 1$  (see Fig. 2a). This results in an unphysical stationary intermediate microstructure instead of complete martensite (Fig. 2b). To eliminate this feature, we returned to the fourth-degree interpolating polynomial for the compressive component of the transformation strain while keeping the fifth-degree polynomial for two tensile components. However, we fixed the only free parameter, which was available in interpolation of all components of the transformation strain tensor. Thus, the theory no longer has free parameters for further development, because increasing the polynomial degree leads to an unacceptable stress-order parameter curve and microstructure. However, the same undesired features may be observed for some of the types of 3D loadings, e.g. with large stresses along the tensile components of the transformations strain tensor, for which the fifth-degree polynomial is used. Consequently, some completely different approaches should be developed in the future, e.g. based on several different polynomials within the  $0 \leq \eta \leq 1$  range, similar to the FEM method.
- (c) The fact that the stress hysteresis strongly depends on the stress state, namely, on the magnitude of the tensile lateral stresses, leads to numerous new phenomena. Thus, the interface width increases and the interface energy decreases with increasing tensile lateral stresses. This produces the possibility of controlling the interface properties, which in turn may produce various scale effects in the microstructure morphology and PT parameters (Levitas and Javanbakht (2011); Levitas (2018a)) when the ratio of two different length-scale parameters (like width of the phase interface and external surface) varies. For instance, applying stresses in the low hysteresis regions leads to some complex microstructures with bands of intermediately phases. Finally, when the instability stresses for the direct and reverse PTs coincide, the interface width diverges, and both direct and reverse transformations occur as a unique homogeneous deformation process without hysteresis and energy dissipation. Due to a lack of interfaces and misfit stresses, damage due to internal elastic stresses should not occur. These properties are perfect for various PT-related engineering applications. In addition, if starting with a two-phase structure under prescribed strain, one increases the tensile lateral stresses, the nanostructure continuously transforms to the homogenous intermediate structure. This means that, in addition to Si I and Si II, an infinite number (continuum) of the homogeneous intermediate phases exist and are in indifferent thermodynamic equilibrium. These phases can be arrested and studied by fixing strain.
- (d) Due to the presence of only one martensitic variant which is strongly incompatible with the austenite, internal stresses and elastic strains, that are quite large, are generated, and the pure geometric crystallographic theory of martensite (Bhattacharya (2004)) is not applicable. Large internal stresses in residual Si I promote a quasi-homogeneous transformation of Si I to Si II, along with growth of Si II bands.
- (e) Stress fields within interfaces exhibit several types of behavior. When stresses in bulk from both sides of interfaces are the same, it is straightforward to define excess stresses and their resultant force, which is an elastic part of the surface tension. When stresses in bulk differ insignificantly, one can make an assumption about the position of the Gibbsian dividing surface and define the interfacial stresses as well. However, we observed the case when stresses vary monotonously across an interface, and they are consequently equivalent to the resultant force and bending couple.
- (f) It is demonstrated that the instability stresses for the initiation of the PTs (i.e.  $\eta > 0$  or  $\eta < 1$ ) are independent of the prescribed stress measure. However, even if they correspond to the maximum of the Cauchy stress and PT can be completed at the fixed Cauchy stress, the first Piola–Kirchhoff stress increases and reaches the maximum for larger strain. If the first Piola–Kirchhoff stress is prescribed, an intermediate small value of  $\eta$  is stabilized after the first instability point, i.e. the PT will not be completed at such stresses. The PT only completes after exceeding the maximum of the first Piola–Kirchhoff stress (the second instability

- point). For the transformation strain-based model, even the Cauchy stress has a local maximum slightly higher than the first instability point, and an intermediate  $\eta$  is stabilized for the prescribed Cauchy stress between the instability and the maximum point. Similarly, the PT completes only after exceeding the maximum of the Cauchy stress. For the logarithmic transformation strain-based model, the Cauchy stress-order parameter curve reduces monotonously and fulfillment of the instability condition for the initiation of the PT (i.e.  $\eta > 0$ ) at fixed Cauchy stress leads to completion of the PT.
- (g) The model based on interpolation of the logarithmic transformation strain has two advantages in comparison with the transformation strain-based model.
- (1) It separates volumetric change and change in shape and corresponding stress-related contributions to the thermodynamic driving force and lattice instability conditions. If the final and initial transformation strain have the same volumetric part, such as variant-variant PT or twinning, the volume is preserved during the entire transformation process for the logarithmic model and varies for the transformation strain-based model.
  - (2) The stress-order parameter curve is monotonous for the logarithmic strain-based model and slightly non-monotonous for the transformation strain-based model (see Fig. 2a), leading to more complex instability and transformation behavior.

Both of these advantages are desirable but not fundamental and mandatory. At the same time, the logarithmic strain-based model generates much larger interfacial stresses than the alternative model (see also Basak and Levitas (2017)). Because they do not allow an alternate complete Si I - Si II band structure to be obtained, like in MD simulations (Levitas et al. (2017a, b)) and with the transformation strain-based model, these stresses are too high. One must find a way to relax these stresses before this model can be successfully used. Note that as we discussed above, interfacial stresses cannot be reduced by changing the interpolation functions because we do not have free parameters and cannot increase the polynomial degree. Finding the correct level of the interfacial stresses from atomistic simulations and reproducing them in PFA is one of the most important problems in PFA.

The current model will be generalized for multivariant martensitic PTs and for multiphase PFA, to be able to include multiple other high-pressure phases of Si. Our model may be also useful for PFA modeling of PTs in other materials, e.g. in Zhu et al. (2017); Mamivand et al. (2014); Paranjape et al. (2016).

## Acknowledgement

The support of NSF (CMMI-1536925 and DMR-1434613), ARO (W911NF-17-1-0225), ONR (N00014-16-1-2079), and Iowa State University (Vance Coffman Faculty Chair Professorship) are gratefully acknowledged. The simulations were performed at Extreme Science and Engineering Discovery Environment (XSEDE), allocations TG-MSS140033 and MSS170015.

## References

- Artemev, A., Wang, Y., Khachaturyan, A.G., 2000. Three-dimensional phase field model and simulation of martensitic transformation in multilayer systems under applied stresses. *Acta Mater.* 48, 2503.
- Artemev, A., Jin, Y., Khachaturyan, A.G., 2001. Three-dimensional phase field model of proper martensitic transformation. *Acta Mater.* 49, 1165.
- Bangerth, W., Hartmann, R., Kanschat, G., 2007. deal.II – a general purpose object oriented finite element library. *ACM Trans. Math Software* 33 (4), 1–27.
- Basak, A., Levitas, V.I., 2017. Interfacial stresses within boundary between martensitic variants: analytical and numerical finite strain solutions for three phase-field models. *Acta Mater.* 139C, 174–187.
- Bhattacharya, K., 2004. Microstructure of Martensite: Why it Forms and How it Gives Rise to the Shape-memory Effect. Oxford University Press, Oxford.
- Boulbitch, A.A., Toledano, P., 1998. *Phys. Rev. Lett.* 81, 838.
- Cui, J., et al., 2006. Combinatorial search of thermoelastic shape-memory alloys with extremely small hysteresis width. *Nat. Mater.* 5 (4), 286–290.
- Fischer, F.D., Waitz, T., Vollath, D., Simha, N.K., 2008. On the role of surface energy and surface stress in phase-transforming nanoparticles. *Prog. Mater. Sci.* 53, 481–527.
- Gibbs, J.W., 1948. The Collected Works of J. Willard Gibbs. Yale University Press, New Haven.
- Hennig, R.G., Wadehra, A., Driver, K.P., Parker, W.D., Umrigar, C.J., Wilkins, J.W., 2010. Phase transformation in Si from semiconducting diamond to metallic beta-Sn phase in QMC and DFT under hydrostatic and anisotropic stress. *Phys. Rev. B* 82, 014101.
- Hill, R., Milstein, F., 1977. Principles of stability analysis of ideal crystals. *Phys. Rev. B* 15, 3087–3096.
- Ichitsubo, T., Tanaka, K., Koiwa, M., Yamazaki, Yo, 2000. Kinetics of cubic to tetragonal transformation under external field by the time-dependent Ginzburg-Landau approach. *Phys. Rev. B* 62, 5435.
- Lekhnitskii, S.G., 1963. Theory of Elasticity of an Anisotropic Elastic Body. Holden-Day Inc.
- Levitas, V.I., 2013. Phase-field theory for martensitic phase transformations. *Int. J. Plast.* 49, 85.
- Levitas, V.I., 2014a. Phase field approach to martensitic phase transformations with large strains and interface stresses. *J. Mech. Phys. Solid.* 70, 154.
- Levitas, V.I., 2014b. Unambiguous Gibbs double surface for nonequilibrium finite-width interface: static equivalence approach. *Phys. Rev. B* 89, 094107.
- Levitas, V.I., 2018a. Effect of the ratio of two nanosize parameters on the phase transformations. Viewpoint article. *Scripta Mater.* 149C, 155–162.
- Levitas, V.I., 2018b. Phase Field Approach for Stress- and Temperature-induced Phase Transformations that Satisfies Lattice Instability Conditions. Part I. General Theory. pp. 30. <https://doi.org/10.1016/j.ijplas.2018.03.007>.
- Levitas, V.I., Javabakhsh, M., 2011. Surface-induced phase transformations: multiple scale and mechanics effects and morphological transitions. *Phys. Rev. Lett.* 107, 175701.
- Levitas, V.I., Preston, D.L., 2002a. Three-dimensional Landau theory for multivariant stress-induced martensitic phase transformations. Part I. Austenite  $\leftrightarrow$  martensite. *Phys. Rev. B* 66 134206(1–9).
- Levitas, V.I., Preston, D.L., 2002b. Three-dimensional Landau theory for multivariant stress-induced martensitic phase transformations. Part II. Multivariant phase transformations and stress space analysis. *Phys. Rev. B* 66 134207(1–15).
- Levitas, V.I., Preston, D.L., Lee, D.W., 2003. Three-dimensional Landau theory for multivariant stress-induced martensitic phase transformations. III. Alternative potentials, critical nuclei, kink solutions, and dislocation theory. *Phys. Rev. B* 68, 134201.
- Levitas, V.I., Lee, D.-W., Preston, D.L., 2006a. Phase field theory of surface- and size-induced microstructures. *Europhys. Lett.* 76 (1), 81–87.
- Levitas, V.I., Preston, D.L., Lee, D.-W., 2006b. Ginzburg-Landau theory of microstructures: stability, transient dynamics, and functionally graded nanophases. *Europhys. Lett.* 75 (1), 84–90.
- Levitas, V.I., Chen, H., Xiong, L., 2017a. Triaxial-stress-induced homogeneous hysteresis-free first-order phase transformations with stable intermediate phases. *Phys.*

- Rev. Lett. 118, 025701.
- Levitas, V.I., Chen, H., Xiong, L., 2017b. Lattice instability during phase transformations under multiaxial stress: modified transformation work criterion. Phys. Rev. B 96, 054118.
- Lindgård, P.A., Mouritsen, O.G., 1986. Theory and model for martensitic transformations. Phys. Rev. Lett. 57, 2458.
- Mamivand, M., Zaem, M.A., El Kadiri, H., 2014. Shape memory effect and pseudoelasticity behavior in tetragonal zirconia polycrystals: a phase-field study. Int. J. Plast. 60, 71–86.
- Milstein, F., Marschall, J., Fang, H., 1995. Theoretical bccfcc transitions in metals via bifurcations under uniaxial load. Phys. Rev. Lett. 74, 2977–2980.
- Paranjape, H.M., Manchiraju, S., Anderson, P.M., 2016. A phase-field Finite element approach to model the interaction between phase transformations and plasticity in shape memory alloys. Int. J. Plast. 80, 1–18.
- Salje, E.K.H., 1990. Phase Transitions in Ferroelastic and Co-elastic Crystals. Cambridge University Press, New York.
- Sutton, A.P., Balluffi, R.W., 1995. Interface in Crystalline Materials. Clarendon Press, Oxford.
- Tüma, K., Stupkiewicz, S., 2016. Phase-field study of size-dependent morphology of austenite-twinned martensite interface in CuAlNi. Int. J. Solid Struct. 97–98, 89–100.
- Tüma, K., Stupkiewicz, S., Petryk, H., 2016. Size effects in martensitic microstructures: finite-strain phase-field model versus sharp-interface approach. J. Mech. Phys. Solid. 95, 284–307.
- Wang, Y., Khachaturyan, A.G., 1997. Three-dimensional field model and computer modeling of martensitic transformations. Acta Mater. 45, 759.
- Wang, J., Yip, S., Phillpot, S.R., Wolf, D., 1993. Crystal instabilities at finite strain. Phys. Rev. Lett. 71, 4182–4185.
- Yan, X., Tan, D., Ren, X., Yang, W., He, D., Mao, H.-K., 2015. Anomalous compression behavior of germanium during phase transformation. Appl. Phys. Lett. 106, 171902.
- Zhu, J., Wu, H., Wang, D., Gao, Y., Wang, H., Hao, Y., Yang, R., Zhang, T., Wang, Y., 2017. Crystallographic analysis and phase-field simulation of transformation plasticity in a multifunctional -Ti alloy. Int. J. Plast. 89, 110–129.